Doctorate Dissertation

博士論文

The roles of PIH-family proteins in vertebrate motile cilia

（脊椎動物の繊毛運動性に関与する PIH ドメインタンパク質ファミリーの機能解析）

A Dissertation Submitted for Degree of Doctor of Philosophy

June 2018

平成 30 年 6 月 博士（理学）申請

Department of Biological Sciences, Graduate School of Science,

The University of Tokyo

東京大学大学院理学系研究科生物科学専攻

Hiroshi Yamaguchi

山口　博史

Contents

Abbreviations

Cryo-ET	cryo-electron tomography
DMT	doublet microtubule
DNAAF	dynein axonemal assembly factor
DNAH	dynein axonemal heavy chain
fps	frames per second
HC	heavy chain
hpf	hours post-fertilization
IAD	inner arm dynein
IC	intermediate chain
N-DRC	nexin-dynein regulatory complex
OAD	outer arm dynein
PCD	primary ciliary dyskinesia
PIH	protein interacting with HSP90
RS	radial spoke

Abstract

In vertebrates, motile cilia/flagella play essential roles in fluid transport and cellular locomotion by generating beating motions. These beating motions are driven by axonemal dyneins, which are huge motor molecules in the cilia/flagella. If axonemal dyneins are defective, cilia/flagella lose motility, leading to a syndrome called primary ciliary dyskinesia (PCD).

Construction of motile cilia/flagella requires cytoplasmic preassembly of axonemal dyneins before transport into cilia. Axonemal dyneins have various subtypes, but the roles of each dynein subtype and their assembly processes remain elusive in vertebrates. For the assembly of different dynein subtypes, the PIH protein family, consisting of four members, has been implicated in this process, although evidence for this idea is sparse.

In my doctoral research, I established zebrafish mutants of all four PIH-protein genes: *pih1d1*, *pih1d2*, *ktu*, and *twister*, and analyzed the structures of axonemal dyneins in mutant spermatozoa by cryo-electron tomography (cryo-ET). Mutations caused the loss of specific dynein subtypes, which was correlated with abnormal sperm motility. I also analyzed the expression patterns of axonemal dynein heavy chain (DNAH) genes and found organ-specific compositions of dynein subtypes, which could explain the organ-specific phenotypes such as the severe motility defects of mutant Kupffer's vesicle cilia (Kupffer's vesicle is a fish ciliated organ equivalent to mammalian embryonic node).

My data demonstrate that all vertebrate PIH proteins are differently required for cilia/flagella motions and the assembly of axonemal dyneins, which allows me to assign specific dynein subtypes to each PIH protein. I also propose zebrafish spermatozoa as a novel model for vertebrate cilia/flagella research, which is capable of genome-editing and cryo-ET structural analysis.

General Introduction

Motile cilia/flagella are hair-like organelles that project from various types of eukaryotic cells. Motile cilia have a microtubule-based structure called an axoneme, consisting of nine peripheral doublet microtubules (DMTs) with or without central-pair microtubules (so called 9+2 or 9+0, respectively). This ciliary architecture is highly conserved among eukaryotes, ranging from protists to mammals. In humans, beating motions of cilia/flagella have important roles in various organs (Figure 1A). In trachea, respiratory epithelial cilia remove debris, which is known as mucociliary clearance (Wanner et al., 1996). In the reproductive system, spermatozoa utilize flagella to swim toward the egg and epithelial cilia in the female reproductive tract contribute to the transport of eggs from fallopian tube to uterus. In the central nervous system, ependymal cilia generate directional cerebrospinal fluid flow which contributes to the homeostasis of the fluid by transporting nutrients and guidance factors (Jiménez et al., 2014). Moreover, motile cilia in embryonic node are required for the settlement of our visceral laterality by generating leftward fluid flow (Nonaka et al., 1998). Because of diverse roles of motile cilia/flagella, their malfunctions often cause PCD, a syndrome characterized by recurrent respiratory infections, male infertility, hydrocephalus, and the inversion of visceral asymmetry (Knowles et al., 2013; Brown and Witman, 2014).

Ciliary motility is driven by axonemal dyneins, which are huge motor molecules aligned along DMTs. Axonemal dyneins have multiple subtypes, such as outer arm dyneins (OADs) and seven different types of inner arm dyneins (IADs; IAD a to g;

Kagami and Kamiya, 1992) (Figure 1B). Biochemical analyses of green algae *Chlamydomonas* revealed that each axonemal dynein consists of multiple subunits (Hom et al., 2011; Sakato and King, 2004). OAD is composed of three heavy chains (α-, β-, and γ-HC), two intermediate chains (IC1 and IC2), and ten light chains. Six types of IADs (IAD a, b, c, d, e, and g) have single HCs with several light chains such as p28, centrin, and actin. IAD f has two heavy chains (f α- and f β-HC), four intermediate chains, and five light chains.

In the process of ciliary construction, axonemal dyneins are synthesized in the cytoplasm and undergo gated entry into the ciliary compartment (Takao and Verhey, 2016). In the cytoplasm, the components of OADs and IADs are detected as preassembled complexes, rather than individual components (Fok et al., 1994; Fowkes and Mitchell, 1998; Viswanadha et al., 2014). This cytoplasmic preassembly of axonemal dyneins requires various proteins collectively called dynein axonemal assembly factors (DNAAFs; Kobayashi and Takeda, 2012; Mitchison et al., 2012) (Figure 2). As cilia/flagella require multiple types of axonemal dyneins for their motions (Kamiya, 1995), proper assembly of each dynein complex is essential for ciliary motility. However, it remains unsolved how different types of axonemal dyneins are assembled. Moreover, the roles of each dynein subtype in cilia/flagella motions remain unclear in vertebrates.

The PIH protein family has been implicated in the preassembly of different dynein subsets in *Chlamydomonas*. However, evidence for this idea is not complete, in particular, in vertebrates. In my doctoral research, I performed systematic functional

analyses of all PIH family proteins using zebrafish, focusing on vertebrate dynein subtypes. In Chapter 1, I established zebrafish mutants of all four PIH genes (genes encoding PIH proteins: *pih1d1*, *pih1d2*, *ktu*, and *twister*) and demonstrated that all vertebrate PIH proteins were required for the assembly of different dynein subtypes. Cryo-ET was applied for the first time to zebrafish sperm, which enabled us to observe the detailed structure of wild-type and mutant axonemal dyneins. In Chapter 2, I investigated organ-specific functions of zebrafish PIH proteins and found more severe motility defects of mutant Kupffer's vesicle cilia. Together with different expression patterns of various DNAH genes, I discuss the organ-specific compositions of axonemal dyneins assembled by PIH proteins.

In this thesis, I identify all vertebrate PIH proteins as DNAAFs, assigning their functions to specific dynein subtypes and to cilia/flagella motions. I combine genome-editing and cryo-ET structural analysis of zebrafish spermatozoa for the first time, providing zebrafish spermatozoa as a novel model for vertebrate cilia/flagella research.

Chapter 1

Functional analyses of all PIH family proteins using zebrafish spermatozoa

Introduction

The PIH family protein, which contains a PIH1-domain, was first identified in budding yeast (*Saccharomyces cerevisiae*) as an interactor of HSP90 and named as Pih1 (Protein Interacting with HSP90; also known as Nop17; Zhao et al., 2005; Gonzales et al., 2005). Yeast Pih1 is required for the assembly of various multi-subunit protein complexes, but is not involved in the assembly of axonemal dyneins, as yeast do not have a cilium. In vertebrates, there are four PIH proteins: PIH1D1, PIH1D2, KTU/DNAAF2, and PIH1D3/TWISTER (Figure 3A). PIH1D1 is the orthologue of yeast Pih1. Similar to yeast, the human PIH1D1 is a subunit of the R2TP complex (RUVBL1, RUVBL2, RPAP3/Tah1, and PIH1D1) which interacts with HSP90 to promote assembly of various protein complexes for cellular activities such as box C/D snoRNP and RNA polymerase II (Kakihara and Houry, 2012).

KTU/DNAAF2 is the first protein that was identified as a DNAAF (Omran et al., 2008). Genetic and biochemical analyses of KTU/DNAAF2 in medaka (Japanese killifish), human, and *Chlamydomonas* revealed that KTU/DNAAF2 is required for the assembly of OAD and a subset of IADs (Omran et al., 2008). Subsequently, the function of *Chlamydomonas* MOT48, a possible orthologue of vertebrate PIH1D1, was reported; MOT48 is one of three PIH proteins in *Chlamydomonas* (MOT48, PF13/KTU, and TWI1) and is involved in the assembly of another subset of IDAs (Yamamoto et al., 2010). These pioneering studies proposed that preassembly of different subsets of axonemal dyneins is mediated by distinct PIH proteins. However, evidence for this

hypothesis is sparse, due to a lack of systematic studies of all PIH proteins. Although PIH1D3/TWISTER recently turned out to be one of the DNAAFs (Dong et al., 2014; Paff et al., 2017; Olcese et al., 2017), the function of vertebrate PIH1D1 and PIH1D2 has not been addressed in terms of ciliogenesis and ciliary motility. Furthermore, two *Pih1d3* paralogues in mice, *Pih1d3* and *Twister2*, are differently expressed in ciliary/flagellar organs (*Pih1d3* for testis, while *Twister2* for both testis and the others; Dong et al., 2014), suggesting a divergence of their functions.

In Chapter 1, I compared the functions of all four vertebrate PIH proteins using one platform, zebrafish spermatozoa. Although zebrafish is often used to analyze the functions of PCD related genes, the detailed structure of their cilia/flagella has not been studied so far. Cryo-ET is suitable to analyze the detailed structure of axonemes, since axonemes are rapidly frozen to preserve molecular structures without chemical fixation or staining, and the 3D structures are reconstructed from images recorded at different angles. I applied cryo-ET for the first time to zebrafish sperm, which enabled us to visualize the detailed structures of axonemal dyneins. I revealed that mutations of each PIH gene caused defects of different subtypes of axonemal dyneins, which was correlated with abnormal sperm motility.

Results

Generation of zebrafish mutants of the *pih1d1*, *pih1d2*, *ktu* and *twister* genes

To find all PIH proteins encoded in the zebrafish genome, I performed BLASTp search with the consensus sequence of PIH proteins as a query. Although teleost fish are known to have undergone an additional genome duplication (Kasahara et al., 2007), only four hits were obtained, similar to the human genome and consistent with a previous report (Yamamoto et al., 2010). I thus conclude that zebrafish has four PIH proteins: Pih1d1, Pih1d2, Ktu, and Twister. Their domain structures are well conserved among vertebrates (Figure 3).

Transcripts of these four PIH genes were all detected in ciliated organs such as Kupffer's vesicle, floor plate, otic vesicle and pronephric duct (Figure 4), suggesting their involvement in ciliary functions. The transcript of *pih1d1* was also detected in the whole body of 12 hpf (hours post-fertilization) embryos (Figure 4A; black asterisk), which is consistent with the reported cellular functions of human PIH1D1 (Kakihara and Houry, 2012). *ktu* was also expressed in brain rudiments at 32 hpf (Figure 4A; black arrowhead). In mouse, KTU function in brain was reported for ciliated ependymal cells (Matsuo et al., 2012). These results suggest that *pih1d2*, *ktu*, and *twister* have cilium-specific functions, while *pih1d1* has ubiquitous cellular functions in addition to ciliary function.

Since DNAAFs including PIH proteins are known to be localized to the cytoplasm (Kobayashi and Takeda, 2012), I examined the subcellular localizations of zebrafish

PIH proteins by immunoblot analysis, using specific polyclonal antibodies made in this study. All PIH proteins were detected in both testis lysate and sperm lysate. However, when spermatozoa were fractionated into sperm heads and flagella, PIH proteins were detected only in the sperm head fraction, indicating that like other DNAAFs, zebrafish PIH proteins are indeed specifically present in the cytoplasm, but not in the flagellar compartment (Figure 5; asterisks).

To analyze the functions of the four PIH proteins in zebrafish, I generated mutant alleles by genome-editing with TALEN (*pih1d1* and *pih1d2*) or CRISPR/Cas9 (*ktu* and *twister*) (Figure 6A-C). Immunoblot analysis confirmed that all mutations resulted in a null of each PIH protein (Figure 6D). Since homozygous mutants of each PIH gene were viable, I established homozygous mutant lines. These were used in the following experiments.

$pih1d1^{-/-}$, $twister^{-/-}$, and double mutant of $pih1d2^{-/-}$;$ktu^{-/-}$ showed abnormal sperm motility

Ciliary functions of PIH genes were examined by observing the motility of mutant spermatozoa using a high-speed camera. Spermatozoa whose heads were attached to a coverslip were selected and subjected to the analyses of beating frequencies and waveforms. Beating frequencies of sperm flagella were measured by sperm kymographs, which were generated by re-slicing the sperm movies as stack images at the mid-region of flagella. Sperm waveforms were analyzed by tracing sperm flagella six times in one beating cycle and shear angle plots, whose slopes represent the size of flagellar bending,

were calculated from each trace of the flagella.

In *pih1d1*$^{-/-}$, spermatozoa showed a slight reduction of beating frequency (Figure 7), and propagation of flagellar bending was disturbed, as slopes of shear angle curves changed between traces (Figure 8B'; asterisk). In *twister*$^{-/-}$, almost all spermatozoa were immotile, but a few were found to be motile with decreased beating frequencies and severely disturbed waveforms (Figure 7; Figure 8E). In *pih1d2*$^{-/-}$ and *ktu*$^{-/-}$, a significant difference was not observed in either beating frequencies or waveforms (Figure 7; Figure 8C,D). I suspected functional compensation of these two genes, and thus generated double mutants of *pih1d2*$^{-/-}$;*ktu*$^{-/-}$. Double mutant spermatozoa exhibited abnormal waveforms; motile in the proximal half, while immotile in the distal half (Figure 8F). In the proximal region, beating frequency was about twice as high as that of wild type (Figure 7B). This could be caused by the reduction of sliding distance of DMTs, rather than the change of the sliding velocity of DMTs, because the slopes of shear angle curves was decreased (Figure 8F'; dotted line), indicating that the bending of the proximal flagella was smaller than that of wild type. I also analyzed the length of sperm flagella, but did not find any significant differences between wild type and PIH gene mutants (Figure 9).

I then analyzed the motility of free swimming spermatozoa by using imageJ plugin of Computer Assisted Sperm Analyzer, which was generated for zebrafish sperm motility analysis (Wilson-Leedy and Ingermann, 2007). In this analysis, traced paths of swimming sperm heads were used to calculate sperm motility (Figure 10A). In all mutants, the ratios of motile (locomotive) spermatozoa were significantly decreased,

and no sperm in *twister*$^{-/-}$ showed significant locomotion (Figure 10B). For motile spermatozoa, swimming velocity did not change in *pih1d1*$^{-/-}$, *pih1d2*$^{-/-}$, and *ktu*$^{-/-}$, but significantly decreased in *pih1d2*$^{-/-}$;*ktu*$^{-/-}$ (Figure 10C). The beating frequencies of sperm heads were decreased in *pih1d1*$^{-/-}$, but increased in *pih1d2*$^{-/-}$;*ktu*$^{-/-}$ (Figure 10D), which is consistent with Figure 7B.

Cryo-ET revealed native ultrastructure of zebrafish sperm axoneme

To observe the ultrastructure of zebrafish axoneme, I applied cryo-ET to zebrafish spermatozoa. The axoneme of zebrafish sperm had the characteristic 9+2 arrangement of DMTs surrounding central-pair microtubules (Figure 11A). To analyze the structure of DMTs in more detail, subtomographic averaging was applied using the 96-nm repeat of DMTs assuming nine-fold rotational symmetry of the axoneme, since I did not detect any obvious heterogeneity of nine DMTs in zebrafish sperm unlike *Chlamydomonas* flagella and sea urchin sperm (Hoops and Witman, 1983; Bui et al., 2012; Lin et al., 2012). The averaged structure of zebrafish DMT exhibited overall similarity to that of other organisms (Figure 11D,E). Thus, based on the well-studied structure of the *Chlamydomonas* axoneme (Bui et al., 2012), I assigned the structures of OADs, seven types of IADs, radial spokes (RSs), and nexin-dynein regulatory complex (N-DRC) in the zebrafish axoneme (Figure 11B,C).

To address the evolutionary conservation and diversity of cilia/flagella, I compared the ultrastructure of zebrafish axoneme to that of *Chlamydomonas* and human axonemes in more detail. Compared with *Chlamydomonas*, zebrafish axoneme does not

have OAD α-HCs and has longer RS3 (Figure 11B,E). A linker between N-DRC and OAD is not observed in the zebrafish axoneme unlike *Chlamydomonas* (Figure 11E; red arrowhead). These features of the zebrafish axoneme are also found in human respiratory cilia (Figure 11D; Lin et al., 2014). The same features were also reported in mouse respiratory cilia (Ueno et al., 2012) and found in sea urchin spermatozoa (Lin et al., 2012), indicating that these features are common among metazoans.

Mutations of each PIH gene caused structural defects of different subtypes of axonemal dyneins

To gain structural insights into abnormal motility of mutant spermatozoa, I observed the structure of mutant axonemes by cryo-ET and subtomographic averaging. Compared to wild type, mutant axonemes exhibited structural defects of various types of axonemal dyneins (later summarized in Figure 22A). IAD c was missing in *pih1d1*$^{-/-}$ (Figure 12A), while no significant difference was observed in *pih1d2*$^{-/-}$ (Figure 12B). In *ktu*$^{-/-}$, smaller IAD c density was observed, suggesting that the structure of IAD c is partially missing in *ktu*$^{-/-}$ spermatozoa (Figure 12C). In *twister*$^{-/-}$, reflecting severe motility defects, OADs and IAD c were missing and smaller IAD g and d were observed (Figure 12D). Intriguingly, in *pih1d2*$^{-/-}$;*ktu*$^{-/-}$, averaging of all DMT particles did not converge into one structure, thus tomograms were classified as follows. I noticed that out of nine tomograms of axonemes, four axonemes had OADs but five lacked OADs. Using this difference, I divided axonemes into two classes (+OAD and -OAD) and averaged, respectively. The +OAD class possessed a full set of axonemal dyneins, except for a

smaller IAD c, like the *ktu*$^{-/-}$ axoneme (Figure 12E). By contrast, the -OAD class lost not only OADs, but also IAD b, c, and e (Figure 12F). However, note that the –OAD class showed faint densities of these IADs in the subtomographic slice (Figure 13B), which suggests that IAD b, c, and e were retained partially in the –OAD class axonemes. Although I found structural defects of axonemal dyneins, no significant defect was observed in other DMT structures, such as RSs and N-DRC, in all mutants I examined.

To correlate the structural defects of mutants with biochemical data, I performed immunoblot analysis of axonemal dynein components (Figure 14). I made specific antibodies against zebrafish Dnah8 (OAD γ-HC) and Dnah2 (IAD f β-HC). Dnai1 is a component of OADs and is also known as IC1. I purchased a commercial antibody against Dnai1. Dnali1 is the orthologue of *Chlamydomonas* p28, which is the subunit of three types of IADs: IAD a, c, and d (Piperno *et al*., 1990; Hom et al., 2011). An antibody against Dnali1 was kindly provided by Dr. Gianni Piperno (anti-p28 antibody; LeDizet and Piperno, 1995).

Consistent with the above structural analysis, Dnah8 and Dnai1 were missing from the axoneme of *twister*$^{-/-}$ (Figure 14; asterisks). In *pih1d2*$^{-/-}$;*ktu*$^{-/-}$, the amount of Dnah8 and Dnai1 was decreased, possibly reflecting the presence of the two types of DMT structures (+OAD and -OAD). Dnah2 was not affected in any mutants, and so was the case of IAD f in the structural analysis. Dnali1 was slightly decreased in *pih1d1*$^{-/-}$, *ktu*$^{-/-}$, and *pih1d2*$^{-/-}$;*ktu*$^{-/-}$ (Figure 14; filled circles), confirming the loss of IAD c (one of three IADs containing p28 in *Chlamydomonas*) in these mutants. In *twister*$^{-/-}$, the structural analysis revealed the loss of IAD c and d (two of three IADs containing p28),

and the amount of Dnali1 was strongly reduced. Interestingly, shifted bands of Dnai1 were observed in *pih1d1*$^{-/-}$ and *pih1d2*$^{-/-}$ (Figure 14; open circles), indicating abnormal modification or truncation of the OAD subunit in these mutants. However, the structure of OADs in these mutants appeared normal as far as my structural analysis showed at the current resolution. Taken together, all biochemical results are largely consistent with our structural data.

pih1d2$^{-/-}$;_ktu_$^{-/-}$ spermatozoa have different axonemal structures between proximal and distal regions

The two types of DMT structures in *pih1d2*$^{-/-}$;*ktu*$^{-/-}$, (Figure 12E,F; +OAD and -OAD classes) led me to examine their distribution in the mutant axoneme. For this, I stained mutant spermatozoa with the anti-Dnah8 (OAD γ-HC) antibody (Figure 15). In wild type, Dnah8 was localized along the entire length of the flagellum. However, in *pih1d2*$^{-/-}$;*ktu*$^{-/-}$, Dnah8 was consistently absent in the distal region, while it remained in the proximal (Figure 15; white arrowhead). Thus, the +OAD class structure was localized in the proximal region, while the -OAD class was in the distal. I also analyzed the localization of Dnah8 in other mutants. Consistent with my structural analysis, in *pih1d1*$^{-/-}$, *pih1d2*$^{-/-}$, and *ktu*$^{-/-}$ spermatozoa, Dnah8 was normally distributed along the entire length of their flagella, while *twister*$^{-/-}$ spermatozoa completely lost Dnah8.

Different structural defects of IADs were also observed between the +OAD and -OAD classes. To assess the distribution of IADs in *pih1d2*$^{-/-}$;*ktu*$^{-/-}$, I analyzed the structure of proximal and distal axoneme directly. Among many cryo-prepared

pih1d2$^{-/-}$;*ktu*$^{-/-}$ axonemes, I found one axoneme suitable for observing both proximal and distal regions by cryo-ET (Figure 16A). Although the obtained subtomograms are noisy due to a smaller number of averaged particles, the DMT structure of a proximal subtomogram possessed OADs and the densities of all IADs, consistent with the structure of +OAD class (Figure 16B,D). On the other hand, the DMT structure of a distal subtomogram lost OADs, IAD b, c, and e, which corresponds to -OAD class (Figure 16C,E). Therefore, the distribution of not only OADs but also IADs is different between the proximal and distal regions in *pih1d2*$^{-/-}$;*ktu*$^{-/-}$ spermatozoa.

Discussion

To perform systematic analyses of all vertebrate PIH proteins, I established zebrafish mutants of all four PIH genes; *pih1d1*, *pih1d2*, *ktu*, and *twister*. In Chapter 1, I focused on zebrafish spermatozoa and analyzed the functions of all PIH family proteins in the sperm motility and in the assembly of axonemal dyneins. Cryo-ET and immunoblot analysis revealed that mutations of each PIH gene caused defects of different dynein subtypes, which was correlated with the abnormal sperm motility. Given that all PIH proteins are specifically localized in the sperm head and not localized in the flagella, I identified all vertebrate PIH proteins (not only Ktu and Twister, but also Pih1d1 and Pih1d2) as DNAAFs.

Loss of specific dynein subtypes in PIH gene mutants causes different abnormal sperm motility

pih1d1$^{-/-}$, *twister*$^{-/-}$ and *pih1d2*$^{-/-}$;*ktu*$^{-/-}$ showed different abnormal sperm motility: *pih1d1*$^{-/-}$, slower beating; *twister*$^{-/-}$, immotile; and *pih1d2*$^{-/-}$;*ktu*$^{-/-}$, increased beating frequency in proximal flagella and immtile in distal flagella. My cryo-ET analysis revealed that in these mutants, different dynein subtypes were lost. Therefore, their distinct motility defects can be explained by the loss of different subtypes of axonemal dyneins. On the other hand, spermatozoa of *pih1d2*$^{-/-}$ and *ktu*$^{-/-}$ appeared to have normal motility, although the structural or biochemical analyses revealed abnormal axonemal dyneins in these mutants. A likely explanation for this discrepancy is that the defects of

axonemal dyneins in *pih1d2*$^{-/-}$ or *ktu*$^{-/-}$ spermatozoa are so subtle that other normal axonemal dyneins can compensate their loss of function. As for *pih1d2*$^{-/-}$ and *ktu*$^{-/-}$, it is also worth noting that the affected axonemal dyneins were different between *pih1d2*$^{-/-}$ (OAD Dnai1) and *ktu*$^{-/-}$ (IAD c), which indicates distinct functions of Pih1d2 and Ktu, although functional compensation of these two genes was also revealed by *pih1d2*$^{-/-}$;*ktu*$^{-/-}$.

Note that in my analysis, the motility of spermatozoa was assessed under the artificial conditions; spermatozoa were allowed to move in the interface between buffer solution and a coverslip (for the sperm waveform analysis) or in the 10 μm thick interface of buffer solution between a glass slide and a coverslip (for the motility analysis of free swimming spermatozoa). These artificial conditions may affect flagellar motility and thus the analysis under physiological conditions (i.e. more thick space of fish breeding water) will be required in the future to reveal the physiological motility of zebrafish normal and mutant spermatozoa.

Sperm axoneme of *pih1d2*$^{-/-}$;*ktu*$^{-/-}$ exhibited distal-specific loss of axonemal dyneins

In *pih1d2*$^{-/-}$;*ktu*$^{-/-}$ spermatozoa, OAD, IAD b, c, and e were missing only from the distal region of the flagella. The distal-specific loss of motility in *pih1d2*$^{-/-}$;*ktu*$^{-/-}$ spermatozoa can be explained by the missing of these axonemal dyneins, since no significant defect was observed in other DMT structures, such as N-DRC, which forms a cross-bridge between DMTs and imposes a load on the DMT sliding driven by axonemal dyneins (Oda et al., 2015). As for the distal-specific missing of axonemal dyneins, one possible

explanation for this phenotype is that the lack of both Pih1d2 and Ktu causes decreased efficiency of axonemal dynein assembly, leading to a shortage of dyneins to be loaded in the distal axoneme. Actually, the axoneme is known to continue elongating by adding flagellar components to its distal end during ciliogenesis (Johnson and Rosenbaum, 1992), and in mature spermatozoa, the transport of flagellar components is highly improbable, because IFT components disappear as spermatozoa mature (San Agustin et al., 2015). Alternatively, the distal and proximal region of zebrafish sperm could differ in the composition of axonemal dyneins. Indeed, *Chlamydomonas* has axonemal dyneins that localize exclusively to the proximal portion of the flagella (Yagi et al., 2009), and human respiratory cilia are known to have two types of OADs, i.e. DNAH11/DNAH5-containing OADs in the proximal and DNAH9/DNAH5-containing OADs in the distal parts (shown in Figure 21B; Fliegauf et al., 2005; Dougherty et al., 2016). Intriguingly, a mutation in the human KTU/DNAAF2 gene strongly affects the assembly of only distal OADs in respiratory cilia (Omran et al., 2008). However, at the moment, I do not have any evidence for the distal-specific dynein composition in zebrafish spermatozoa. Immunofluorescent staining showed that Dnah8 is present along the entire length of zebrafish sperm flagella (Figure 15). Further analyses with *pih1d2*$^{-/-}$;*ktu*$^{-/-}$ spermatozoa could shed light on the structural and functional difference between distal and proximal regions of vertebrate spermatozoa.

Chapter 2

Different compositions of axonemal dyneins between zebrafish sperm flagella and Kupffer's vesicle cilia

Introduction

In vertebrates, motile cilia/flagella play important roles of fluid transport and cellular locomotion in various organs. Despite having a conserved basic morphology, these cilia/flagella vary in motility patterns among organs; asymmetric planner beating for tracheal cilia, symmetric planar oscillation for sperm flagella, and conical rotational movement for embryonic node cilia. 9+0 arrangement of microtubules have been implicated in the rotational movement of cilia, since mouse node cilia and eel sperm flagella have 9+0 configuration and exhibit rotational motility (Nonaka et al., 1998; Woolley, 1998, 1997). In zebrafish, however, both olfactory placode cilia (asymmetric planner beating) and Kupffer's vesicle cilia (rotational movement) have 9+2 arrangement of microtubules (Wloga et al., 2009; Kramer-Zucker et al., 2005), suggesting other molecular or physical factors in the determination of ciliary motility patterns. As for molecular differences between ciliary types, organ-specific compositions of OAD HCs were reported between sperm flagella and respiratory cilia in humans (shown in Figure 21B; Fliegauf et al., 2005; Dougherty et al., 2016), and mouse *Pih1d3* was reported as a testis-specific gene (Dong et al., 2014).

In Chapter 2, to assess the organ-specific functions of PIH proteins, I compared the phenotypes of PIH gene mutants between sperm flagella and Kupffer's vesicle cilia. Kupffer's vesicle is orthologous to the mammalian embryonic node. In Kupffer's vesicle, epithelial cells project mono-cilia that show rotational motility to produce leftward fluid flow inside the organ (Figure 17A,B). Like in the mouse node, this

leftward flow is required for the determination of visceral asymmetry, and thus defects of Kupffer's vesicle cilia cause abnormal left-right patterning of the fish (Essner et al., 2005). In medaka fish, loss of Ktu cause immotile Kupffer's vesicle cilia and randomized left-right patterning (Omran et al., 2008).

I found that in *pih1d2*$^{-/-}$ and *ktu*$^{-/-}$, Kupffer's vesicle cilia showed more severe motility defects compared to sperm flagella, indicating organ-specific functions of these genes. To correlate these phenotypes to ciliary components, I also analyzed expression patterns of various DNAH genes and found organ-specific compositions of axonemal dyneins in zebrafish.

Results

Kupffer's vesicle cilia showed different ciliary phenotypes from sperm flagella

Kupffer's e vesicle cilia have rotational motility to produce directional fluid flow inside the organ. To describe this ciliary motility in PIH gene mutants, I categorized motion patterns into three classes: rotating, irregular, and immotile (Figure 17C,D). Rotational frequencies were measured from rotating class cilia (Figure 17E). The resulting left-right patterning of embryos was assessed by observing the direction of heart looping (normally rightward; Figure 18).

In *pih1d1*$^{-/-}$, rotational frequencies of cilia were significantly reduced, but almost all cilia were motile and the ratio of heart-looping reversal was not largely affected. By contrast, in *twister*$^{-/-}$ and *pih1d2*$^{-/-}$;*ktu*$^{-/-}$, all cilia were immotile, leading to complete randomization of their left-right patterning. In *pih1d2*$^{-/-}$ and *ktu*$^{-/-}$, the proportions of rotating class cilia were decreased to ~40% and ~15%, respectively, with reduced rotational frequencies, resulting in significant levels of heart-looping defects (Figure 18A). Regarding the structure and localization of axonemal dyneins, due to technical difficulties, I was unable to apply cryo-ET and immunohistochemistry with anti-dynein antibodies to the axonemes of Kupffer's vesicle cilia.

Together with Chapter 1, I conclude that all PIH genes are essential for the motility of both sperm flagella and Kupffer's vesicle cilia. Intriguingly, however, in *pih1d2*$^{-/-}$ and *ktu*$^{-/-}$, only Kupffer's vesicle cilia showed motility defects, while sperm flagella beat normally, indicating that Pih1d2 and Ktu have organ-specific functions.

Testis and Kupffer's vesicle showed different expression patterns of DNAH genes

The organ-specific phenotypes of PIH mutants could reflect organ-specific compositions of axonemal dyneins. To address this, I performed whole-mount *in situ* hybridization of various DNAH genes. Zebrafish have three OAD β-HC genes: *dnah9*, *dnah9l*, and *dnah11*, and two OAD γ-HC genes: *dnah5* and *dnah8*. As for IAD, *dnah2* is an IAD f β-HC gene, and *dnah3* and *dnah7l* are other IAD HC genes. The gene correspondence of dynein heavy chains among zebrafish, human, and *Chlamydomonas* are summarized in Table 1, based on the comprehensive analysis of dynein phylogeny by Kollmar (2016).

Zebrafish embryos and testes showed distinct expression patterns of DNAH genes (Figure 20A). When comparing Kupffer's vesicle and testis, *dnah11* expression was specifically detected in Kupffer's vesicle, while *dnah8* and *dnah3* were specifically detected in testis (Figure 20B). At embryonic stages, *dnah9l* and *dnah8* were detected only in the otic vesicle and pronephric duct, respectively, which also suggested specific combinations of DNAH genes in these organs. These results indicate that components of axonemal dyneins are indeed organ-specific.

Intriguingly, however, Kupffer's vesicle and floor plate, whose cilia exhibit similar rotational motility (Kramer-Zucker et al., 2005), showed the same expression patterns of DNAH genes (Figure 20A). It is likely that the same transcriptional regulation is required in Kupffer's vesicle and floor plate to construct similar types of cilia.

Discussion

In Chapter 2, to investigate the organ-specific functions of PIH proteins, I compared ciliary phenotypes of PIH gene mutants between sperm flagella and Kupffer's vesicle cilia. Although all PIH genes were essential for normal motility of both sperm flagella and Kupffer's vesicle cilia, *pih1d2*$^{-/-}$ and *ktu*$^{-/-}$ showed more severe motility defects of Kupffer's vesicle cilia than sperm flagella, indicating organ-specific functions of PIH1d2 and Ktu. I also found different compositions of axonemal dyneins between sperms and Kupffer's vesicle cilia. Given that all four PIH genes/proteins are expressed in the two organs (Figure 4A; Figure 5), phenotypic differences between *pih1d2*$^{-/-}$ and *ktu*$^{-/-}$ could be accounted for by the different compositions of axonemal dyneins.

Different compositions of axonemal dyneins between ciliated organs

Expression analysis of DNAH genes suggested that the composition of axonemal dyneins differed between sperm flagella and Kupffer's vesicle cilia. In sperm flagella, Dnah9/Dnah8-containing OADs could be most abundant, since Dnah8 (OAD γ-HC) is present along the entire length of sperm flagella (Figure 15) and the expression of only *dnah9* was detectable as for OAD β-HC gene in testis (Figure 20). On the other hand, in Kupffer's vesicle cilia, the axonemes seem to consist of Dnah9/Dnah5-containing OADs and/or Dnah11/Dnah5-containing OADs (Figure 20; Figure 21A). I also found that *dnah3* (IAD HC gene) are differentially expressed between testis and Kupffer's vesicle (Figure 20). It is tempting to speculate that the dynein compositions vary

depending on the pattern of ciliary beating, as cilia and flagella of the two organs exhibit the different mode of movement, planar oscillation for sperm flagella and rotation for Kupffer's vesicle cilia, although different physical conditions of the external fluid could also affect the different motion patterns of sperm flagella and Kupffer's vesicle cilia.

Materials and Methods

Zebrafish maintenance

Zebrafish were maintained at 28.5°C on a 13.5/10.5 hours light/dark cycle. Embryos and larvae were raised at the same temperature in 1/3 Ringer's solution (39 mM NaCl, 0.97 mM KCl, 1.8 mM $CaCl_2$, and 1.7 mM HEPES, pH 7.2). Developmental stages of embryos and larvae are described according to hpf at 28.5°C and the morphological criteria by Kimmel et al. (1995). For embryos used in whole-mount *in situ* hybridization, 200 μM 1-phenyl-2-thiourea was added to 1/3 Ringer's solution to delay pigmentation.

Identification of zebrafish PIH proteins

PIH1 domain is registered as PF08190 in the Pfam database. To find all PIH proteins in the zebrafish genome, BLASTp search was performed with the consensus sequence of the PIH1 domain (pfam08190). Four proteins were identified as a match: Pih1d1 (NP_001153400.1, E value = 2.66e-27), Pih1d2 (NP_001008629.1, E value = 2.08e-9), Ktu (NP_001028272.1, E value = 2.37e-31), and Twister (also known as Pih1d3; NP_001002309.1, E value = 4.16e-5). Paralogues of each match were also checked, since teleost fish are known to have undergone an additional genome duplication. BLASTn and tBLASTn search were performed using each PIH sequence as a query, however only the proteins containing the query sequence were a hit in E value <10. Therefore zebrafish have four PIH proteins: Pih1d1, Pih1d2, Ktu, and Twister.

Zebrafish genome-editing

Zebrafish genome-editing was performed according to previous reports of TALEN (Bedell et al., 2012) or CRISPR/Cas9 (Gagnon et al., 2014). Target sites of my genome-editing are as follows: *pih1d1* (TALEN left), GTTGAACACGAGCAGAAACAA; *pih1d1* (TALEN right), TGAAGCAGAAGTTGTTGGTA; *pih1d2* (TALEN left), TACAGGAGCTTCATTCAG; *pih1d2* (TALEN right), TGAGTGAAACTCGGCTCCC; *ktu* (CRIPSR gRNA), GGAGATCCGGCCACAGCTGG; *twister* (CRISPR gRNA), GGATAATGATGAGGAAGAAG. Genomic DNA was extracted from the developing embryos and target loci were amplified to check the mutations by sanger-sequencing. After identifying founder fish, each mutant line underwent back-cross twice to remove the effect of possible off-target mutations.

Sperm treatment

Zebrafish sperm was expelled by gently squeezing the sides of the fish, and collected in Hank's buffer (137 mM NaCl, 5.4 mM KCl, 0.25 mM Na_2HPO_4, 0.44 mM KH_2PO_4, 1.3 mM $CaCl_2$, 1.0 mM $MgSO_4$, and 4.2 mM $NaHCO_3$). For the fractionation of sperm head and flagella, spermatozoa were passed through a 26 gauge needle 20 times in Hank's buffer with 2 mg/ml BSA, and the separated heads and flagella were collected by centrifugation (head: 400 *g*, 3 min; flagella: 9000 *g*, 3 min). For purification of sperm axonemes, sperm heads and membranes were removed by adding 2% Nonidet P-40 to Hank's buffer, and demembranated axonemes were collected by centrifugation (10000 *g*,

3 min), then resuspended in HMDEKAc buffer (30 mM HEPES at pH 7.2, 5 mM $MgSO_4$, 1 mM dithiothreitol, 1 mM EGTA, and 50 mM CH_3COOK).

Sperm motility analyses

To observe proper motility, spermatozoa were kept on wet ice until analyzed, and used within 1 hour of sperm collection. Zebrafish spermatozoa were inactive in Hank's buffer, but were activated by adding abundant amount of 1/5× Hank's buffer. Sperm motilities were observed under bright-field conditions using an inverted microscope (DMI6000B; Leica) and a high-speed camera (HAS-L1; Detect). For waveform analysis, spermatozoa whose heads were attached to the coverslip were selected and waveforms of flagella were filmed at 1000 fps (frames per second). On the other hand, when using imageJ plugin of Computer Assisted Sperm Analyzer, 2 mg/ml of BSA was added to buffers to prevent sperm from attaching to the glass and free swimming spermatozoa were filmed at 200 fps. ImageJ plugin of Computer Assisted Sperm Analyzer was used as previously reported (Wilson-Leedy and Ingermann, 2007) with slight modifications: spermatozoa were prepared on glass slides with 10 μm spacers (200A10; Kyodo giken chemical), and covered with coverslips to provide a consistent fluid depth. In this analysis, eight independent experiments with two times of 1 sec observations were performed to obtain sixteen technical replicates.

Cryo-preparation of zebrafish sperm axoneme

Purified sperm axoneme were incubated with anti-α-tubulin antibody (1:10000 dilution;

T9026; Sigma-Aldrich) for 15 min at 4°C in HMDEKAc buffer, and then with anti-mouse antibody conjugated with 15 nm colloidal gold (final 1:50 dilution; EM.GMHL15; BBInternational) and 15 nm colloidal gold conjugated with BSA (final 1:5 dilution; 215.133; Aurion) were added. Holey carbon grids were glow discharged before use to make them hydrophilic. 5 µl of axoneme solution was loaded onto the grid, and then excess liquid was blotted away with filter paper to make a thin film of the solution. Immediately after, the grid was plunged into liquid ethane at −180°C for a rapid freeze of the solution. Blotting and freezing were automatically performed by an automated plunge-freezing device (EM GP; Leica). Cryo-prepared grids were stored in liquid nitrogen until observation using the electron microscope.

Cryo-image acquisition and image processing

Cryo-prepared grids were transferred into a transmission electron microscope (JEM-3100FEF; JEOL) with a high-tilt liquid nitrogen cryotransfer holder (914; Gatan), and kept at −180°C. Images of single axis tilt series were collected using a 4,096 × 4,096–pixel CMOS camera (TemCam-F416; TVIPS) and automated acquisition software (EM-TOOLs; TVIPS). Tilt series were acquired by a stepwise rotation of the sample from −60 to 60° in 2.0° increments. The total electron dose was limited to approximately 100 e/Å^2 for an individual tilt series to avoid radiation damage of the sample. Images were recorded at 300 keV, with 8.8µm defocus, at a magnification of 30,000× and a pixel size of 7.2 Å. An in-column Ω energy filter was used to enhance image contrast in the zero-loss mode with a slit width of 20 eV. The tilt series images

were aligned and reconstructed into 3D tomograms using IMOD software (Kremer et al., 1996). Alignment and averaging of subtomograms were conducted by custom Ruby-Helix scripts (Metlagel et al., 2007) and PEET (Particle Estimation for Electron Tomography) software suite (Nicastro et al., 2006), using a 96-nm repeat of DMT as one particle assuming a nine-fold rotational symmetry of the axoneme. Effective resolutions were determined by Fourier shell correlation with a cutoff value of 0.143. For the visualization of tomographic slices or 3D structures, 3dmod program (IMOD software) or isosurface rendering of UCSF Chimera package (Pettersen et al., 2004) were used, respectively.

Immunofluorescence microscopy

Spermatozoa in Hank's buffer were attached to the wells of an 8-well glass slide (TF0808; Matsunami). After washing out excess sperm, attached spermatozoa were briefly demembranated using 1% Nonidet P-40 for 2 min. Specimens were fixed with 2% paraformaldehyde/Hank's buffer for 10 min at room temperature, followed by treatment with cold acetone and methanol (-20°C). After rehydration with PBST (phosphate buffered saline containing 0.1% Tween-20), specimens were treated with blocking buffer (2% normal goat serum, 1% cold fish gelatin in PBST). Immunostaining was performed with anti-acetylated tubulin antibody (1:500 dilution; T6793; Sigma-Aldrich) and anti-Dnah8 antibody (1:50 dilution; generated in this study) as primary antibodies. Alexa Fluor 488 Donkey anti-mouse IgG (1:250 dilution; ab150105; Abcam) and Alexa Fluor 555 Donkey anti-rabbit IgG (1:250 dilution; ab150074;

Abcam) were used as secondary antibodies with 2.5 μg/ml DAPI (Wako) for nuclear staining. Specimens were mounted with Fluoro-KEEPER Antifade Reagent (Nacalai tesque) and observed with a fluorescence microscope (BX60; Olympus) and a CCD camera (ORCA-R2; Hamamatsu).

Kupffer's vesicle cilia analysis

Embryos developing Kupffer's vesicle were selected at 12 hpf and dechrionated before observations. To align the orientations, embryos were embedded in 0.8% of low gelling temperature agarose (Sigma-Aldrich) with 1/3 Ringer's solution. Motility of Kupffer's vesicle cilia were observed under the bright-field conditions using an inverted microscope (DMI6000B; Leica) and a high-speed camera (HAS-L1; Detect) at 1000 fps.

RNA probe synthesis

The sequences of zebrafish PIH genes and DNAH genes were subcloned into pCRII-TOPO plasmid (Invitrogen). From the constructed plasmids, RNA probes were synthesized using SP6 or T7 RNA polymerase (Roche) with DIG RNA Labeling Mix (Roche). RNAs were purified using RNeasy Mini Kit (Qiagen). Sequences of primers used in the construction of plasmids are summarized in Table 2.

Whole-mount *in situ* hybridization

Dechorionated embryos or dissected testes were fixed with 4% paraformaldehyde (PFA)

in PBST, and then stored in methanol at −20°C. After rehydration with PBST, specimens were treated with proteinase K and re-fixed with 4% PFA/PBST solution. Hybridization was performed overnight at 63°C in hybridization buffer (750 mM NaCl, 75 mM trisodium citrate, 500 μg/ml torula tRNA, 50 μg/ml Heparin, 50% formamide, and 0.1% Tween-20) with digoxigenin-labeled RNA probes. Hybridized specimens were washed with 50% formamide/2×SSCT (saline sodium citrate containing 0.1% Tween-20) followed by 2× SSCT and 0.2× SSCT, then treated with AP-conjugated anti-digoxigenin Fab fragments (1:4000 dilution; Roche) in blocking solution (150 mM NaCl, 100 mM maleic acid at pH 7.5, 5% blocking reagent (Roche), 5% normal goat serum, and 0.1% Tween-20) at 4°C overnight. After washing with MABT (150 mM NaCl, 100 mM maleic acid at pH 7.5, and 0.1% Tween-20), signals were developed using BM-purple (Roche). When desired intensities of staining were obtained, reactions were stopped by stopping solution (PBST containing 1 mM EDTA) and 4% PFA/PBST. Before observations, specimens were transferred into 80% glycerol/PBS to make them transparent. For some embryos, to show stained organs clearly, posterior regions were flat-mounted or yolk was removed. Images were taken by a stereoscopic microscope (MVX10; Olympus) and a CCD camera (DP73; Olympus).

Antibodies

Sequences encoding full length of zebrafish PIH proteins (Pih1d1, Pih1d2, Ktu, and Twister) were subcloned into the pColdI plasmid vector (Takara). Sequences encoding zebrafish Dnah8 (amino acid 895-1402) and Dnah2 (amino acid 802-1378) were

subcloned into the pGEX-6P-2 plasmid vector (GE Healthcare). Recombinant polypeptides were purified from transformed *E.coli* lysate using Ni-NTA Agarose (Qiagen) for PIH proteins or Glutathione Sepharose 4B (GE Healthcare) for Dnah8 and Dnah2. Polyclonal antibodies against each purified polypeptide with tag were raised by immunization of rabbits. Antibodies were affinity purified from serum by the antigens before use. Sequences of the primers used in the antigen production are summarized in Table 2. Other antibodies used are as follows: anti-Dnai1 rabbit polyclonal antibody (GTX109719; GeneTex), anti-Dnali1 rabbit polyclonal antibody (anti-p28 antibody; kindly provided by Dr. Gianni Piperno; LeDizet and Piperno, 1995), anti-α-tubulin mouse monoclonal antibody (T9026; Sigma-Aldrich), and anti-acetylated tubulin mouse monoclonal antibody (T6793; Sigma-Aldrich).

Immunoblot analysis

Proteins were separated by SDS-PAGE in 5-20% gradient polyacrylamide gels (Nacalai Tesque) and transferred onto polyvinylidene difluoride (PVDF) membranes (Millipore). After blocking with 5% skim milk (Nacalai Tesque) in TBST (Tris-buffered saline containing 0.1% Tween-20), membranes were incubated with primary antibodies, followed by several washes and incubation with secondary antibodies (goat anti rabbit/mouse IgG antibody peroxidase conjugated; Sigma-Aldrich). Protein signals were visualized by ECL Select Western Blotting Detection Reagent (GE Healthcare) and observed using luminescent image analyzer (ImageQuant LAS4000mini; GE Healthcare).

Statistics

Data with biological/technical replicates are shown with mean (bar graphs) ± SD (error bars). Statistical significances between WT and each mutant were tested by a two-tailed Dunnett's test, and P value < 0.05 was considered to indicate a significant difference.

Accession numbers

The averaged subtomograms of zebrafish DMTs in this study are available at the EMDataBank (http://www.emdatabank.org/) under the following accession numbers: WT, EMD-6954; *pih1d1*$^{-/-}$, EMD-6955; *pih1d2*$^{-/-}$, EMD-6956; *ktu*$^{-/-}$, EMD-6957; *twister*$^{-/-}$, EMD-6958; *pih1d2*$^{-/-}$;*ktu*$^{-/-}$ (+OAD class), EMD-6959; and *pih1d2*$^{-/-}$;*ktu*$^{-/-}$ (-OAD class), EMD-6960.

General Discussion

In the process of ciliary construction, the PIH family proteins have been implicated in the preassembly of different subsets of axonemal dyneins, but there had been insufficient evidence to support this idea before my study. I performed the systematic analyses of all PIH proteins using zebrafish, and demonstrated that all of vertebrate PIH proteins (including two uncharacterized ciliary factors, Pih1d1 and Pih1d2) are required for cilia/flagella motions and assembly of axonemal dyneins. Each PIH protein was responsible for the construction of different subsets of axonemal dyneins, suggesting that the cytoplasmic assembly pathways for different axonemal dyneins are mediated by distinct PIH proteins.

PIH proteins are required for the constructions of specific subsets of axonemal dyneins

Cryo-ET and biochemical analyses revealed that the PIH proteins are required for the assemblies of specific subsets of axonemal dyneins (Figure 23A): Pih1d1 for OAD (Dnai1 construction) and IAD c; Pih1d2 and Ktu for OAD, IAD b, c, and e; and Twister for OAD, IAD c, g, and d. In *Chlamydomonas*, the mutation of KTU/PF13 affected the assembly of OAD and IAD c, while the mutation of MOT48 affected the assembly of OAD, IAD b, c, d, and e (Yamamoto et al., 2010). Although the affected subtypes of axonemal dyneins are not the same, the mutations of PIH genes resulted in the loss of specific subsets of axonemal dyneins in both organisms. Remarkably, OAD and IAD c

are most sensitive to the mutations of various PIH genes in both zebrafish and *Chlamydomonas*. Consistent with this, Dong et al. (2014) suggested that the assembly of OAD proceeds in a stepwise manner mediated by different PIH proteins. This might also be the case for IAD c, though no experimental evidence has been obtained (Figure 23B).

In my research, IAD a or f were not affected in any of the PIH mutants (Figure 23A), which was essentially the same as in *Chlamydomonas* mutants of KTU/PF13 and MOT48. This suggests that these axonemal dyneins are assembled independently of PIH proteins. Alternatively, multiple PIH proteins redundantly participate in their assembly. In any case, IAD a or f are unlikely to be constructed automatically, because a defect of DYX1C1 (a known DNAAF other than PIH family proteins; Tarkar et al., 2013) affects the normal assembly of all types of IADs in *Chlamydomonas* (Yamamoto et al., 2017). Double, triple or quadruple mutants of PIH genes will be needed to answer this question.

Comparison of zebrafish PIH protein functions with other reports

The phenotypes of zebrafish PIH gene mutants are summarized in Figure 22. PIH1D1 has been known to serve as a component of R2TP complex, which has various important cellular functions (Kakihara and Houry, 2012), but the role of PIH1D1 in vertebrate development remains poorly understood. Zebrafish *pih1d1*$^{-/-}$ mutants were viable and exhibited only ciliary defects as far as I observed. Thus, Pih1d1 could be mostly redundant in cellular functions. In fact, yeast *PIH1*-deletion cells were also

reported to be viable (Gonzales et al., 2005), like zebrafish *pih1d1*$^{-/-}$.

Accumulated knowledge about DNAAFs has suggested the involvement of R2TP-like complex in the process of axonemal dynein assembly (Li et al., 2017). I identified Pih1d1 as a novel DNAAF, which strongly supports this idea. Since KTU and PIH1D3 are also suggested to participate in R2TP-like complexes (Tarkar et al., 2013; Olcese et al., 2017), each of PIH proteins may serve as a component of R2TP-like complexes. Intriguingly, my expression analysis of PIH genes suggested that *pih1d2*, *ktu*, and *twister* have cilium-specific functions, while *pih1d1* has ubiquitous cellular functions in addition to the ciliary function (Figure 4). Further analysis of binding partners of PIH proteins will provide insights into the mechanism of how PIH1D1 promote the assembly of various types of protein complexes and how distinct PIH proteins modulate the assembly of different types of axonemal dyneins.

It was surprising that the spermatozoa of zebrafish *ktu*$^{-/-}$ showed normal motility, since abnormal sperm motility was reported in both human *KTU/DNAAF2*$^{-/-}$ patients and medaka *ktu* mutants (Omran et al., 2008). This suggests that the function of Ktu and other PIH proteins in zebrafish could have diverged during evolution. Intriguingly, double mutants of *pih1d2*$^{-/-}$;*ktu*$^{-/-}$ showed phenotypes similar to those of the medaka *ktu* mutant, in terms of complete loss of ciliary motility in Kupffer's vesicle (Figure 17C,D) and expansion of pronephric ducts (Figure 19). Furthermore, the waveform of *pih1d2*$^{-/-}$;*ktu*$^{-/-}$ spermatozoa (Figure 8F) highly resembles that of medaka *ktu* mutant spermatozoa (bends do not propagate to the tip of the sperm tail; Omran et al., 2008). The function of medaka Ktu is thus partially shared by Ktu and Pih1d2 in

zebrafish. Such functional divergence of PIH proteins was also reported in human and mouse; human *PIH1D3* has functions in various ciliated organs (Paff et al., 2017; Olcese et al., 2017), while mouse *Pih1d3* is a testis-specific gene (Dong et al., 2014). *Twister2* (paralogue of mouse *Pih1d3*) is expressed in various ciliated organs including testis in mice, but is not able to rescue the loss of *Pih1d3* in testis. Therefore, PIH proteins tend to be functionally diverse and sometimes interchangeable, even though they stay in the category of DNAAFs.

Zebrafish spermatozoa as a novel model for vertebrate cilia/flagella research

The protists *Chlamydomonas* and *Tetrahymena* are the most popular species used in motile cilia/flagella research, due to their abundance of ciliary mutants and easy access to their ciliary structures. At the same time, to analyze the mechanisms of human PCD, vertebrate models have also been explored. In this context, zebrafish is often used to analyze the functions of PCD related genes. However, previous studies with zebrafish did not address the detailed structure of their cilia/flagella. In this thesis, I investigated the functions of all PIH family proteins by combining zebrafish genome-editing and cryo-ET in zebrafish spermatozoa. I found zebrafish spermatozoa a good (or promising) vertebrate cilia/flagella model, since they can be collected without killing adult male fish (see Materials and Methods), while in mice, collections of spermatozoa or tracheal cilia require dissection of these organs. Therefore, my approach using zebrafish spermatozoa with cryo-ET is novel and has provided an excellent platform with which analyze vertebrate motile cilia/flagella.

Table 1. Correspondence of DNAH genes/proteins among zebrafish, human, and *Chlamydomonas*.

	gene/protein names		
	zebrafish	human	*Chlamydomonas*
OAD HCs			OAD α (DHC13)
	Dnah9	DNAH9	OAD β (DHC14)
	Dnah11	DNAH11	
	Dnah9l		
		DNAH17	
	Dnah5	DNAH5	OAD γ (DHC15)
	Dnah8 (Dnah5l)		
		DNAH8	
IAD f HCs	Dnah10	DNAH10	IAD fα (DHC1)
	Dnah2	DNAH2	IAD fβ (DHC10)
IAD HCs	Dnah3	DNAH3	IAD a (DHC6) IAD b (DHC5) IAD c (DHC9) IAD e (DHC8) minor var. DHC11 minor var. DHC4
	Dnah7	DNAH7	
	Dnah12	DNAH12	
	Dnah1	DNAH1	IAD d (DHC2)
	Dnah7l (Dnah6)	DNAH6	IAD g (DHC7)
		DNAH14	minor var. DHC3

Table 2. Primer sequences used in this study

purpose	name	Sequence
probes for *in situ* hybridization	pih1d1.F	GAACCGGAACAGTCAGTGAA
	pih1d1.R	TAGGGCACAAAAACGGAAAC
	pih1d2.F	GTGAGTCCAAGTAGGCTATT
	pih1d2.R	GGATAAACAAGAGTGAACTATTT
	ktu.F	GACGCGCTGTTCACCGGAGC
	ktu.R	GGATCCGCCAGCTGTGGCC
	twister.F	AGAGCAGGACATTCACTTCA
	twister.R	TTGTCTATCTTTCTCTCTGTTTCC
	dnah9.F	ATGTATGGAGTCTGTGGATGCAAAG
	dnah9.R	ACATGGCCGTACAGCAGGAA
	dnah9l.F	CGCGTGGACTTCATTAGAG
	dnah9l.R	TTTGACCGTAAGGCCTG
	dnah11.F	GTGTCAATATTTTTTAACAAGGTGT
	dnah11.R	AATATTGGACAGTTGTCGATCA
	dnah5.F	AAATACCTCTGTCGAATCACTG
	dnah5.R	ATCCTGTGGAGCCAATCC
	dnah8.F	ACAGAAAACGAAGAGTCTCCTC
	dnah8.R	ATCCATAAGGCTGCAGAAG
	dnah2.F	ATGGCTGACCCAGAGACC
	dnah2.R	CTCAGAATGGAACAGATTGTACAC
	dnah3.F	AGGTATTTATACTATGTCACGGAGG
	dnah3.R	AGTGACTTCACTTGTGTGTTTCA
	dnah7l.F	ATGTATTCTTTTCAGAAAGGACATC
	dnah7l.R	AGCATCTTCTTCAAGAATTTCCT
antigen generation	pih1d1_Ag.F	ATGTCTGAGGCACTCATCATG
	pih1d1_Ag.R	TCACAAAGACACGACTGGC

pih1d2_Ag.F	ATGGCAATCCATGGCTAT
pih1d2_Ag.R	TCATAATACATTTACCGTCACATT
ktu_Ag.F	ATGGACGCGGACAGACTG
ktu_Ag.R	TGCTTCCAGTTGGACTGA
twister_Ag.F	ATGGAGGGTCTCGCGTCC
twister_Ag.R	TCAGGTCAGATTAATGCAGTC
dnah8_Ag.F	TATTTCATAGGTTGTGTGTACAAG
dnah8_Ag.R	TTCACGTGGCGGCAAACC
dnah2_Ag.F	AGCGCCTTTATCAATGACTG
dnah2_Ag.R	GATGATCTTCTTAAACTGCTCA

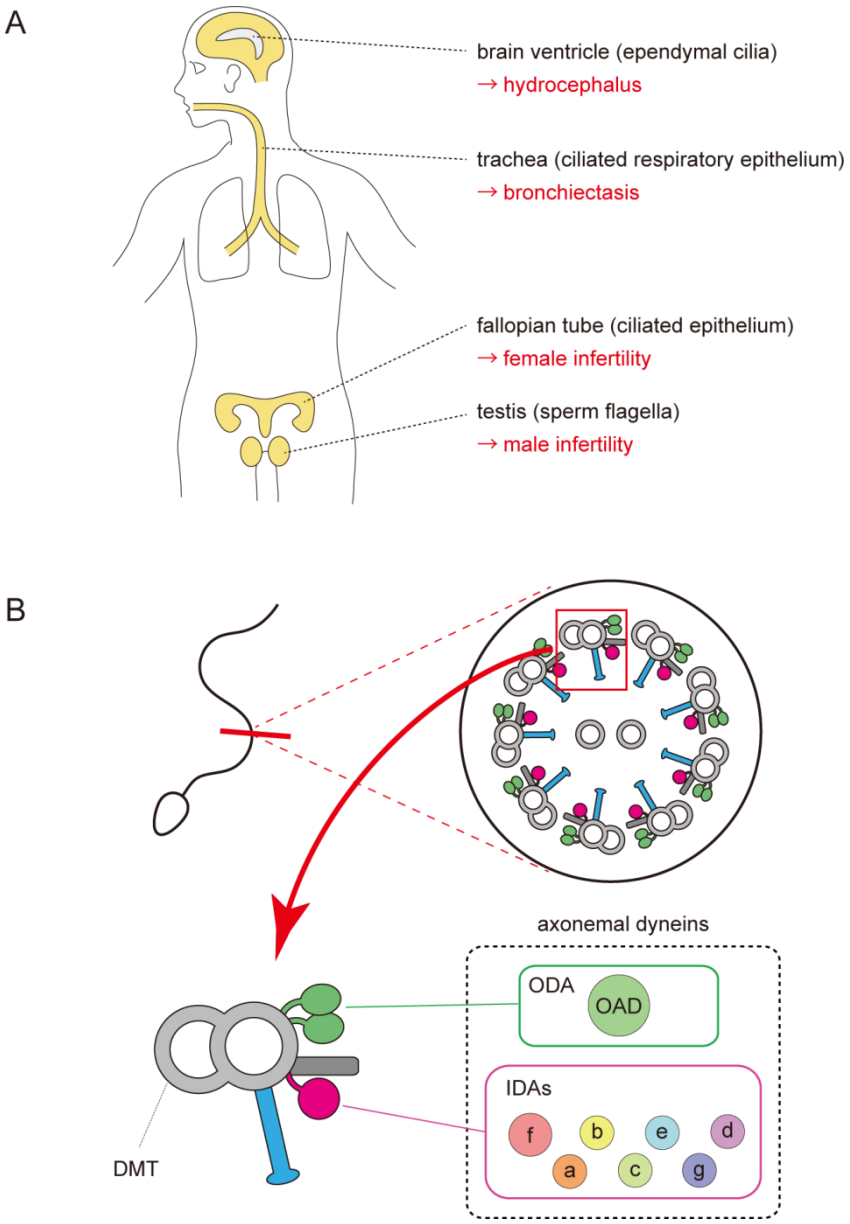

Figure 1. Human ciliated organs and ciliary architecture

(A) Schematic picture of ciliated organs in human body. Red letters indicate PCD phenotypes in respective organs. (B) Upper: transverse section of motile cilia (sperm flagella) representing 9+2 structure of microtubules. Lower: detailed structure of a DMT with axonemal dyneins. Axonemal dyneins have multiple subtypes, such as OAD and seven different types of IADs (IAD a to g).

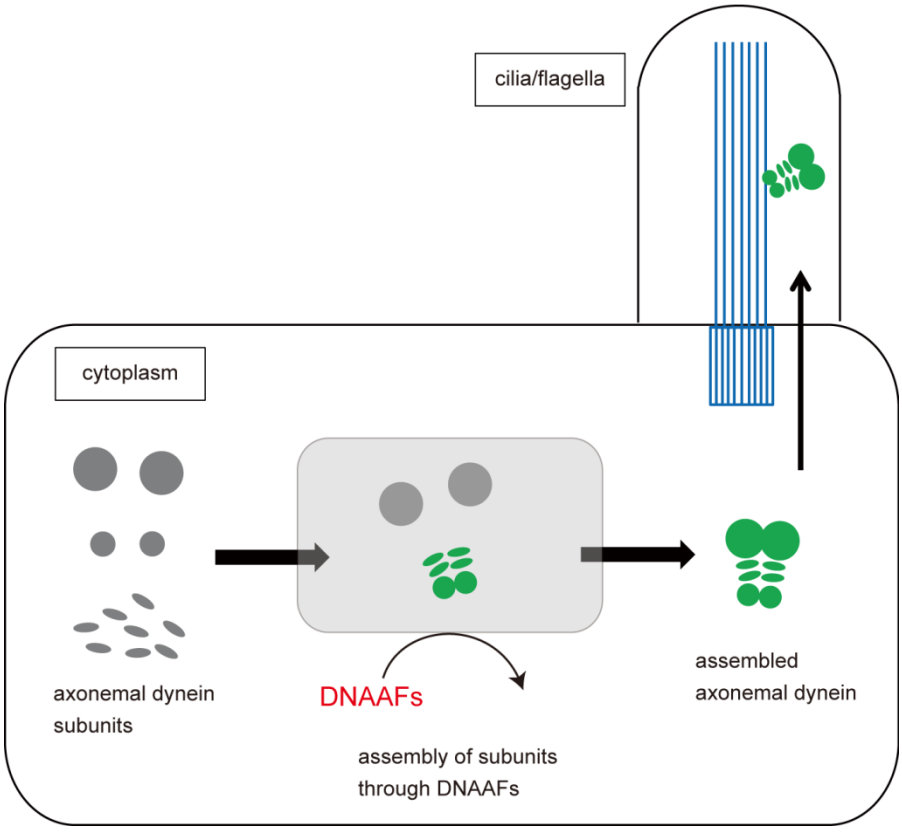

Figure 2. Axonemal dyneins are pre-assembled in the cytoplasm

Diagram of the assembly process of an axonemal dynein complex. In the process of ciliary construction, axonemal dynein subunits are pre-assembled in the cytoplasm before transport into cilia. This cytoplasmic preassembly requires various proteins collectively called DNAAFs.

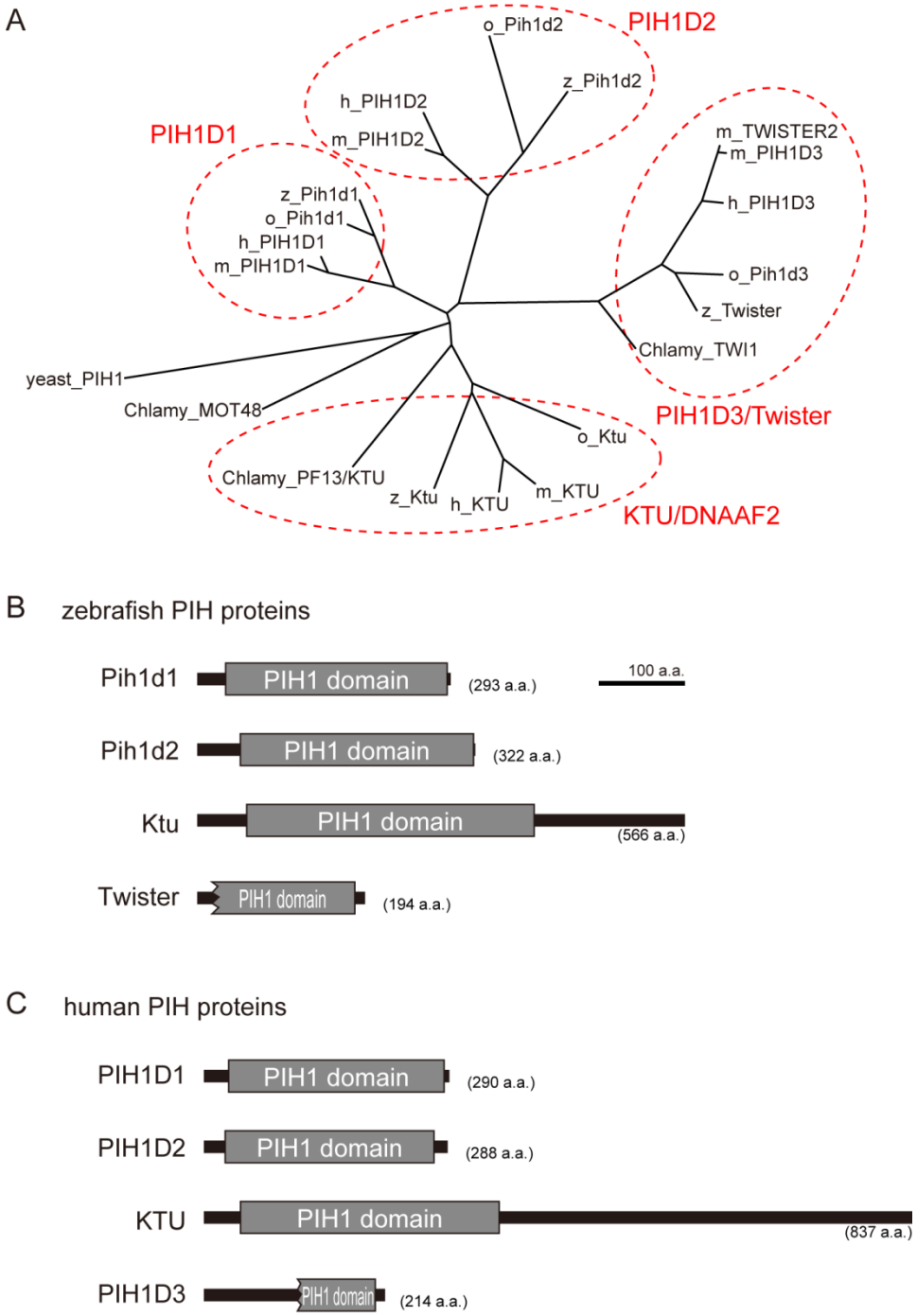

Figure 3. Vertebrates have four PIH family proteins

(A) Phylogenetic tree of PIH proteins in yeast, *Chlamydomonas*, and vertebrates. Amino acid sequences were aligned by MAFFT program with FFT-NS-i option (Katoh and Standley, 2013) and evolutionary distances were calculated using neighbor-joining (Saitou and Nei, 1987). yeast, *Saccharomyces cerevisiae*; Chlamy, *Chlamydomonas*

reinhardtii; z, zebrafish (*Danio rerio*); o, medaka (*Oryzias latipes*); m, *Mus musculus*; h, *Homo sapiens*. (B and C) Domain structures of PIH proteins in (B) zebrafish and (C) human. Protein motifs were obtained by SMART or Pfam analyses.

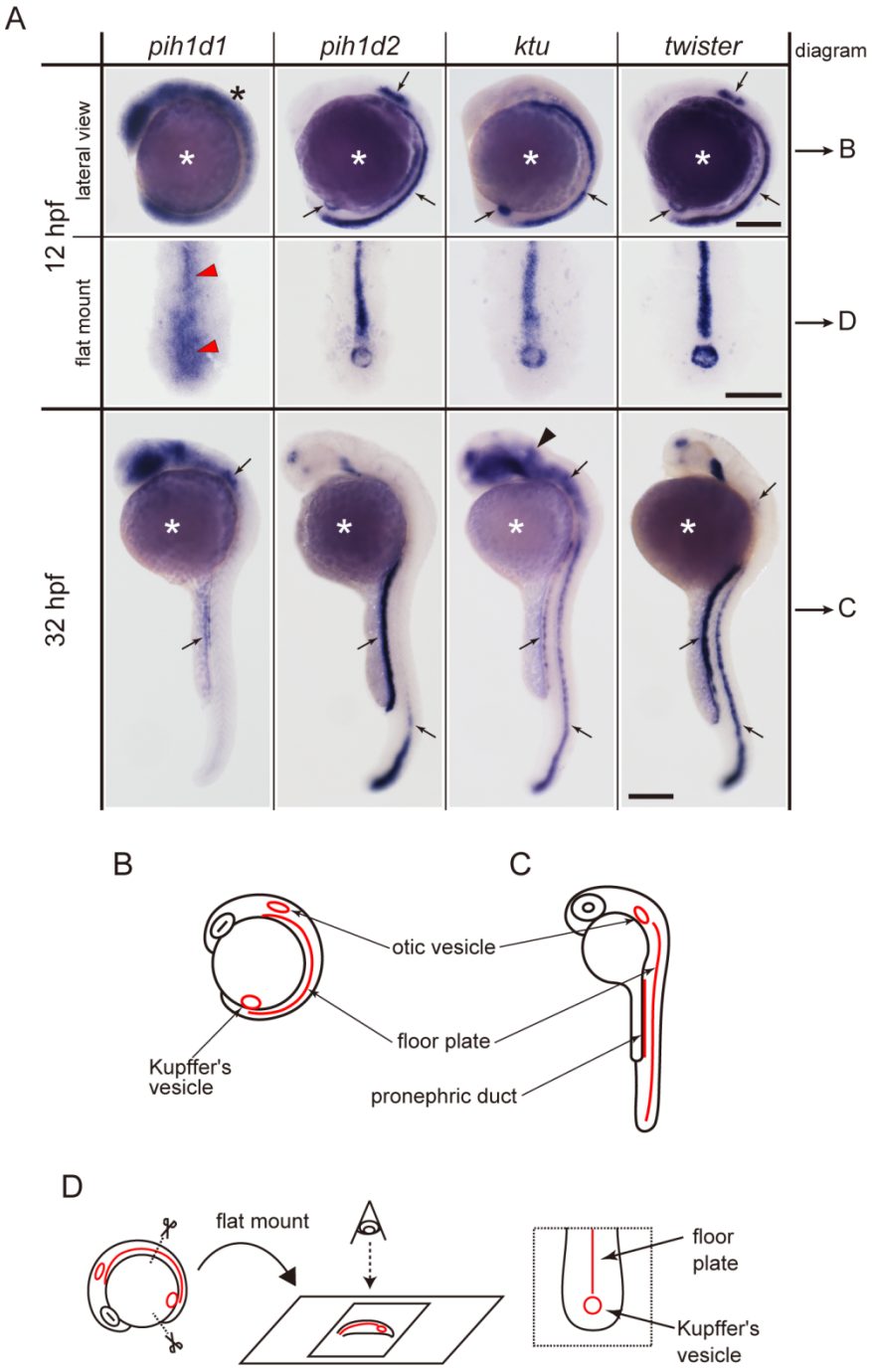

Figure 4. Zebrafish PIH genes, *pih1d1*, *pih1d2*, *ktu*, and *twister*, were expressed in ciliated organs

(A) Whole-mount *in situ* hybridization of PIH genes. Arrows in lateral views indicate expression of PIH genes in ciliated organs (Kupffer's vesicle, floor plate, otic vesicle, and pronephric duct). Flat mount preparations show dorsal views of the posterior

regions of 12 hpf embryos. *pih1d1* was ubiquitously expressed in 12 hpf embryos (black asterisk) containing Kupffer's vesicle and floor plate (red arrowheads). *ktu* was also expressed in brain rudiments at 32 hpf (black arrowhead). White asterisks: non-specific staining of yolk. Scale bars: 200 μm. (B and C) Diagrams of zebrafish embryos at (B) 12 hpf and (C) 32 hpf, showing typical ciliated organs. (D) Left: preparation procedure of flat mount. Right: diagram of Kupffer's vesicle and floor plate in flat-mounted embryos.

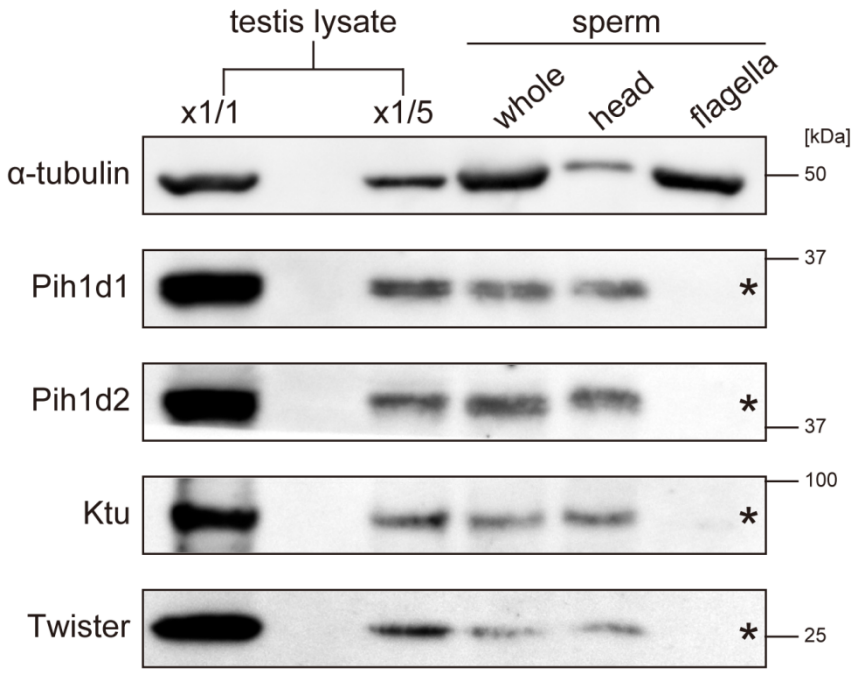

Figure 5. Zebrafish PIH proteins are not localized in the flagellar compartment

Immunoblot of PIH proteins. Although PIH proteins are detected in the testis lysate, whole sperm fraction, and sperm head fraction, none of the PIH proteins were detected in the sperm flagella fraction (asterisks). α-tubulin: control.

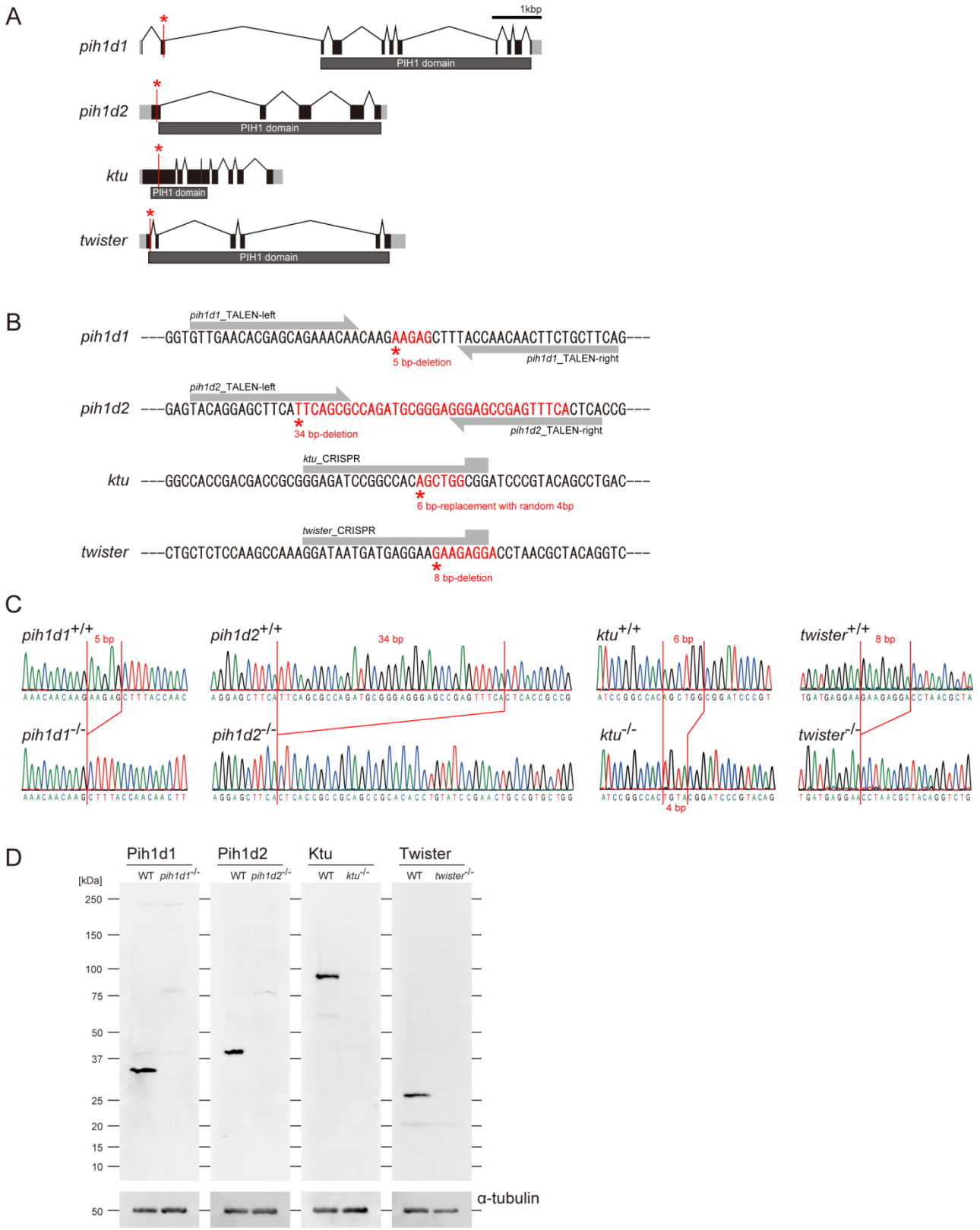

Figure 6. PIH gene mutants were established by genome-editing

(A) Genomic organization of PIH genes in zebrafish. Black: exons. Gray: untranslated regions. Red asterisks indicate the target sites of my genome-editing. (B) Target sequences of my genome-editing. Induced mutations changed the sequences shown in red. (C) Sanger sequencings of WT and PIH gene mutants around the target sites of genome-editing. (D) Immunoblot of testis lysate of WT and PIH gene mutants. Induced mutations caused null of each PIH protein. α-tubulin: control.

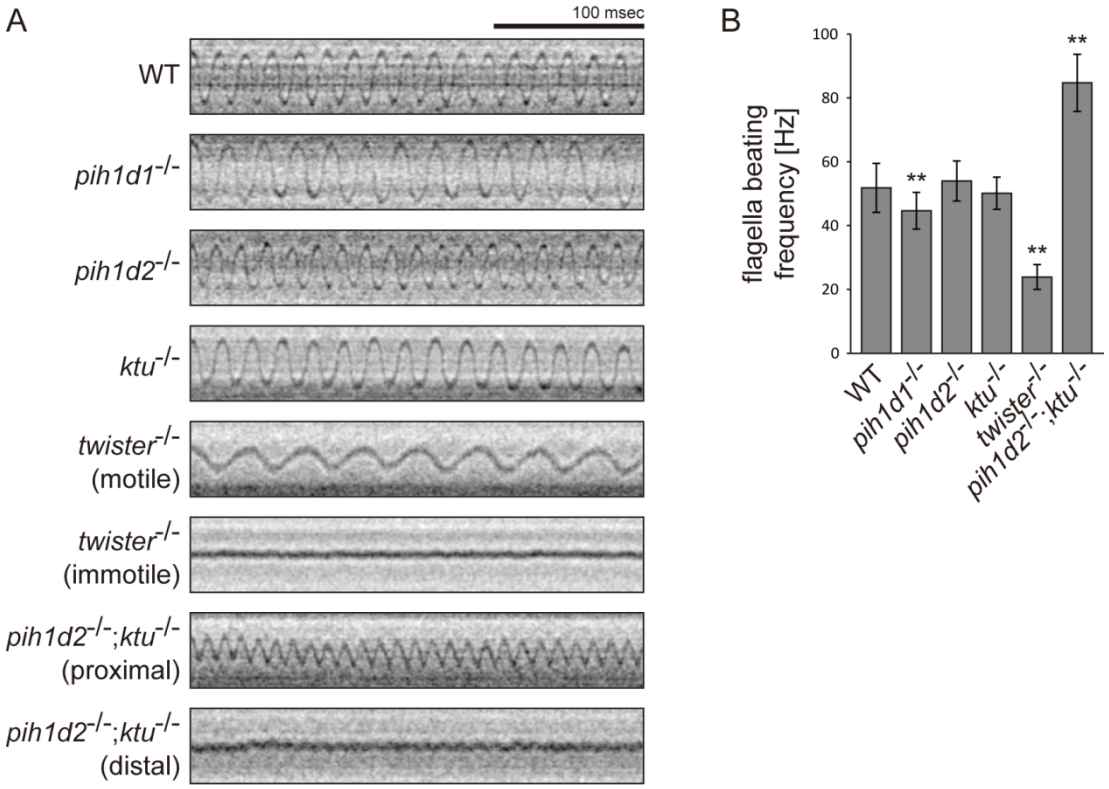

Figure 7. Mutations of PIH genes caused abnormal beating frequency of sperm flagella

Beating of sperm flagella was observed using a high-speed camera at 1000 fps. (A) Typical kymographs of sperm flagella. (B) Beating frequencies of sperm flagella were measured by sperm kymographs. Kymographs of *pih1d2*$^{-/-}$;*ktu*$^{-/-}$ were obtained from the proximal region of sperm flagella, as distal flagella were immotile. Number of samples: WT, 23; *pih1d1*$^{-/-}$, 23; *pih1d2*$^{-/-}$, 26; *ktu*$^{-/-}$, 15; *twister*$^{-/-}$, 8; and *pih1d2*$^{-/-}$;*ktu*$^{-/-}$, 14.

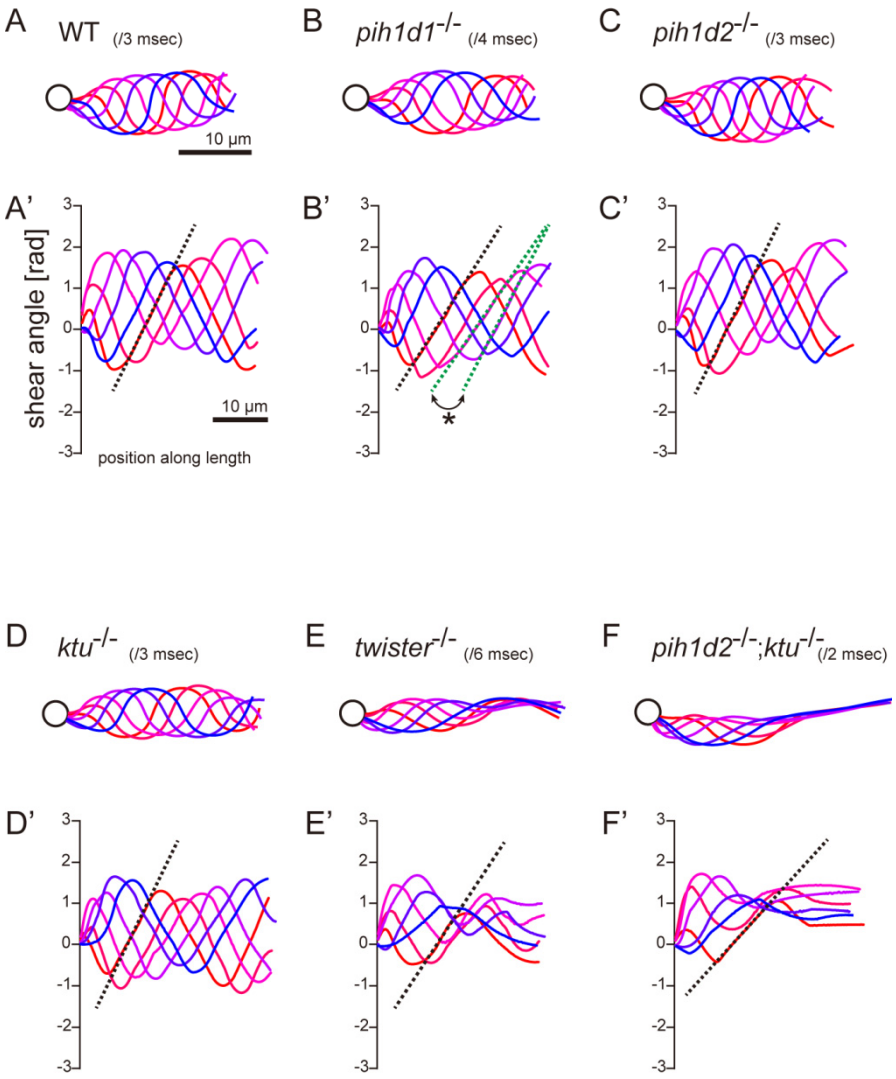

Figure 8. Mutations of PIH genes caused abnormal waveforms of sperm flagella

Waveform of sperms flagella was observed using a high-speed camera at 1000 fps. (A-F) Sperm waveforms were traced six times in one beating cycle and overlaid. Intervals are as follows: WT, 3 msec; *pih1d1*$^{-/-}$, 4 msec; *pih1d2*$^{-/-}$, 3 msec; *ktu*$^{-/-}$, 3 msec; *twister*$^{-/-}$, 6 msec; and *pih1d2*$^{-/-}$;*ktu*$^{-/-}$, 2 msec. Traces are painted in a color gradient of from red (first traces) to blue (sixth traces). (A'-F') Shear angles of beating flagella were calculated from each trace of A-F. Slopes of dotted lines represent the size of flagellar bending. An asterisk with green dotted lines in B' shows unstable propagation of flagellar bending in *pih1d1*$^{-/-}$ sperm.

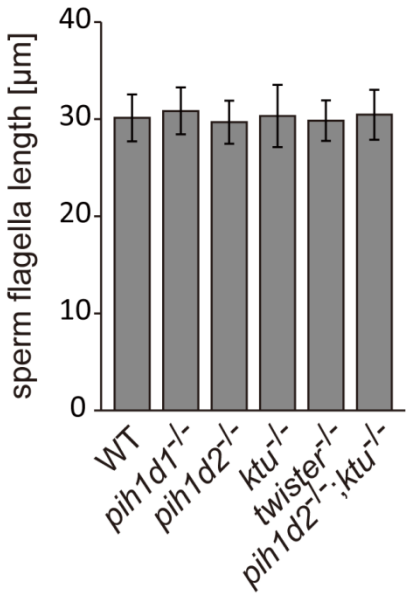

Figure 9. Length of sperm flagella was not affected by the mutations of PIH genes

Immunofluorescent staining of sperm flagella with acetylated tubulin antibodies was performed to measure the length of the flagella. Number of samples: WT, 129; *pih1d1*$^{-/-}$, 64; *pih1d2*$^{-/-}$, 78; *ktu*$^{-/-}$, 84; *twister*$^{-/-}$, 81; and *pih1d2*$^{-/-}$;*ktu*$^{-/-}$, 80. Bar graphs show mean ± SD. Significant differences (p-value < 0.05) were not detected in a Dunnett's test of each mutant against WT.

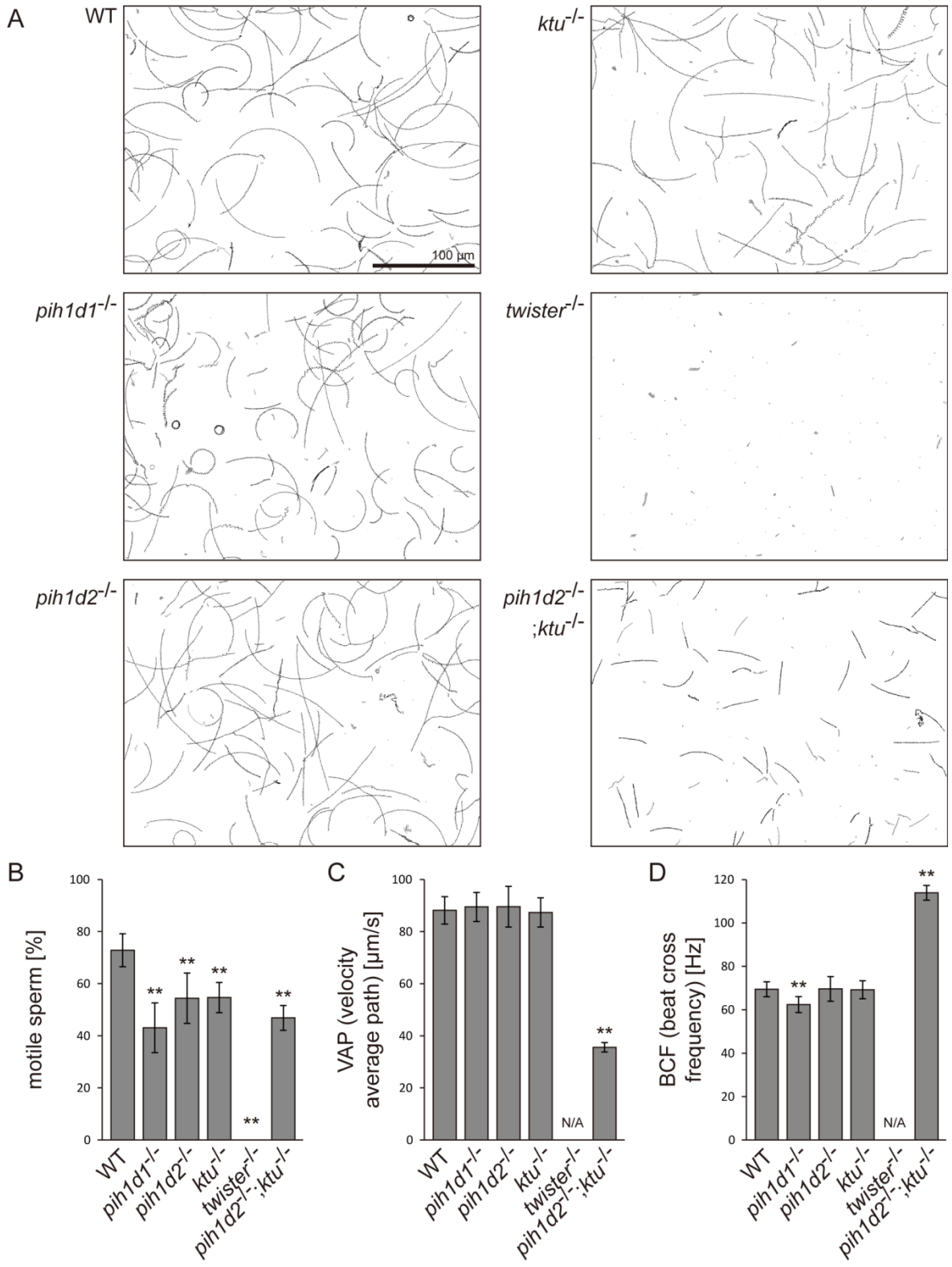

Figure 10. Motility analysis of free swimming spermatozoa using imageJ plugin of Computer Assisted Sperm Analyzer

Motilities of free-swimming spermatozoa were observed using a high-speed camera at 200 fps and analyzed by imageJ plugin of Computer Assisted Sperm Analyzer. For each zebrafish line, more than 1,200 spermatozoa were observed in total with sixteen technical replicates. Spermatozoa with less than 20 μm/s velocities were considered immotile. (A) Typical traced paths of sperm heads. Black: traced paths of motile spermatozoa. Gray: traced paths of immotile (velocity < 20 μm/s) spermatozoa. (B) Ratio of motile (locomotive) sperm. (C) Velocity of spermatozoa on averaged paths. Averaged paths were constructed by connecting the points of averaged sperm positions of coordinating 33 frames. (D) Frequencies at which sperm heads crossed their averaged paths. Bar graphs show mean ± SD. **: p-value < 0.01 in Dunnett's test of each mutant against WT.

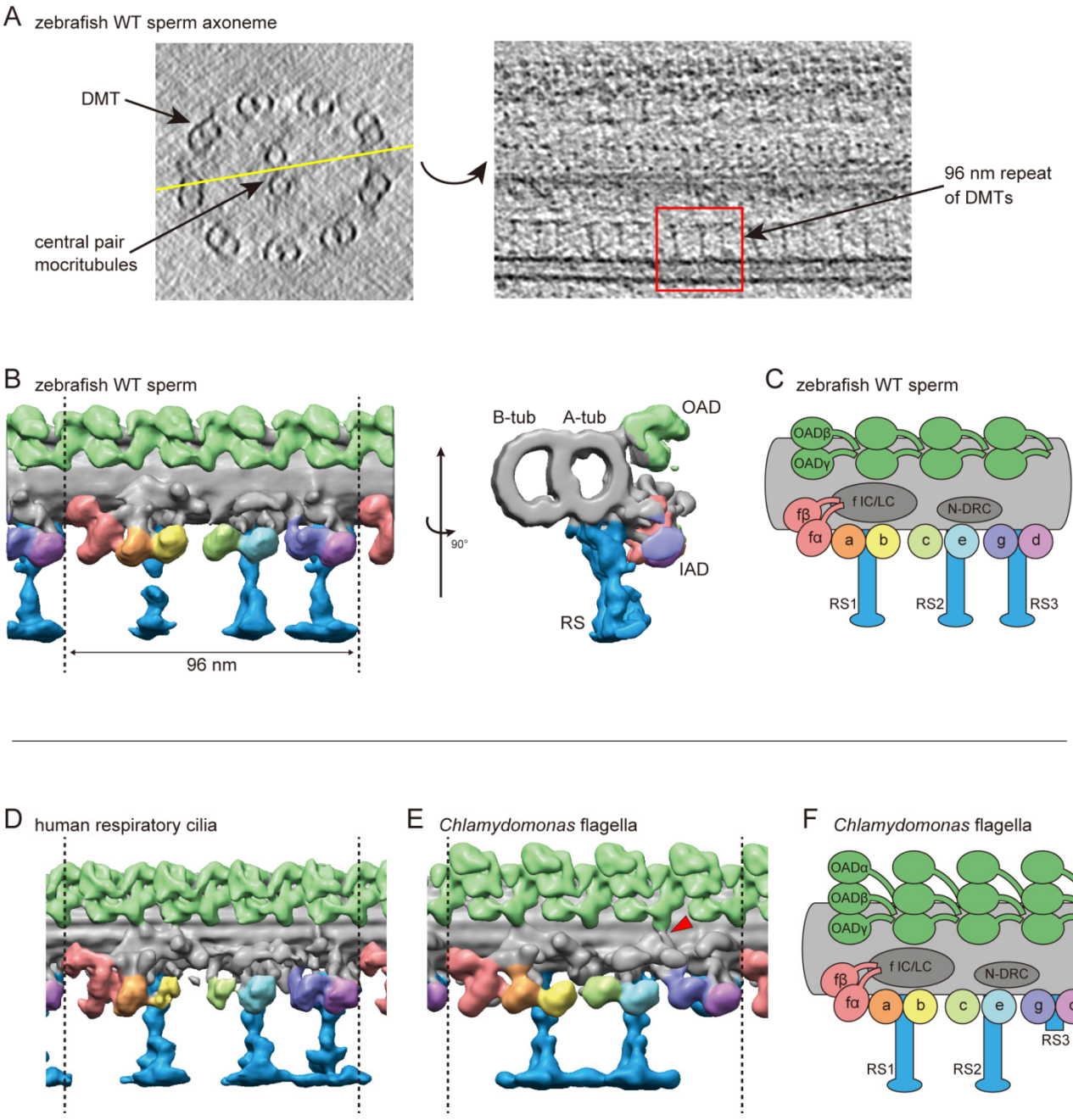

Figure 11. Native ultrastructure of zebrafish sperm axoneme exhibited overall similarity to that of other organisms

(A) Tomographic slices (20 nm thick) of WT sperm axoneme. Left: cross-section (base-to-tip view). Right: longitudinal section at the location indicated by the yellow line in the left-hand image. (B) DMT structure of native zebrafish sperm. Left: side view. Right: base-to-tip view. A-tub and B-tub: A- and B-tubule of DMT, respectively. (C)

Diagram of the DMT structure of zebrafish sperm. f IC/LC means IAD f intermediate chain and light chain complex. (D) DMT structure of human respiratory cilia (EMD-5950; Lin et al., 2014). (E) DMT structure of *Chlamydomonas* flagella (DMT 2-8 averaged; EMD-2132; Bui et al., 2012). Red arrow indicates a linker between N-DRC and OAD. (F) Diagram of the DMT structure of *Chlamydomonas* flagella. Green, OADs; red, IAD f; orange, IAD a; yellow, IAD b; light-green, IAD c; cyan, IAD e; indigo, IAD g; violet, IAD d; blue, RSs.

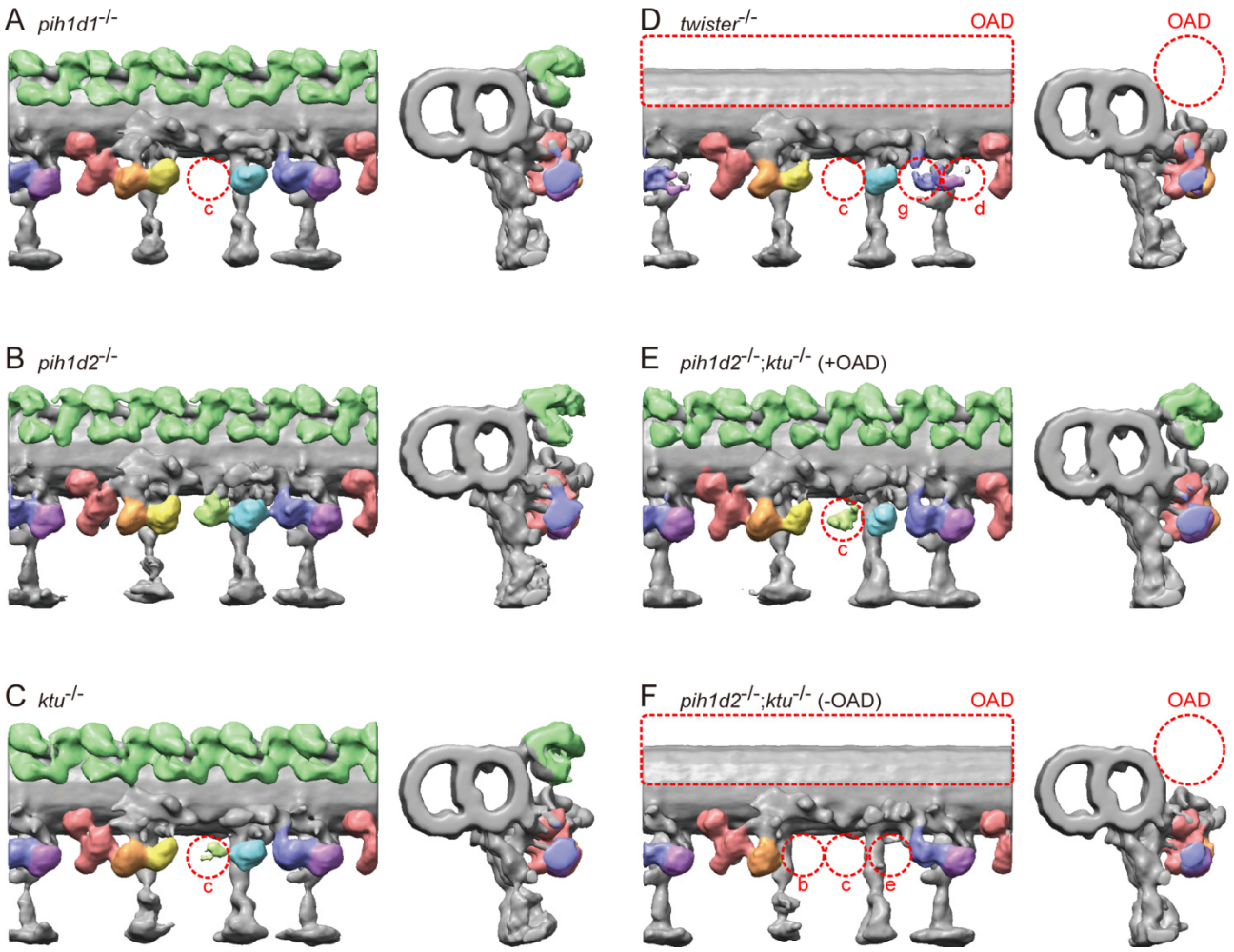

Figure 12. Cryo-ET revealed structural defects of axonemal dyneins in mutant spermatozoa

(A-F) DMT structures of PIH gene mutant spermatozoa. For *pih1d2*$^{-/-}$;*ktu*$^{-/-}$, E (+OAD) and F (-OAD) represent subtomograms from axonemes with or without OADs, respectively. Red circles indicate the defects of axonemal dyneins. Green, OADs; red, IAD f; orange, IAD a; yellow, IAD b; light-green, IAD c; cyan, IAD e; indigo, IAD g; violet, IAD d; blue, RSs.

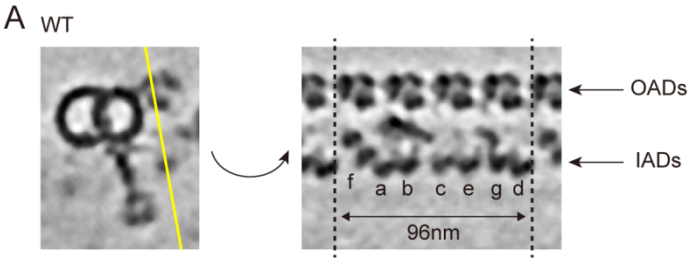

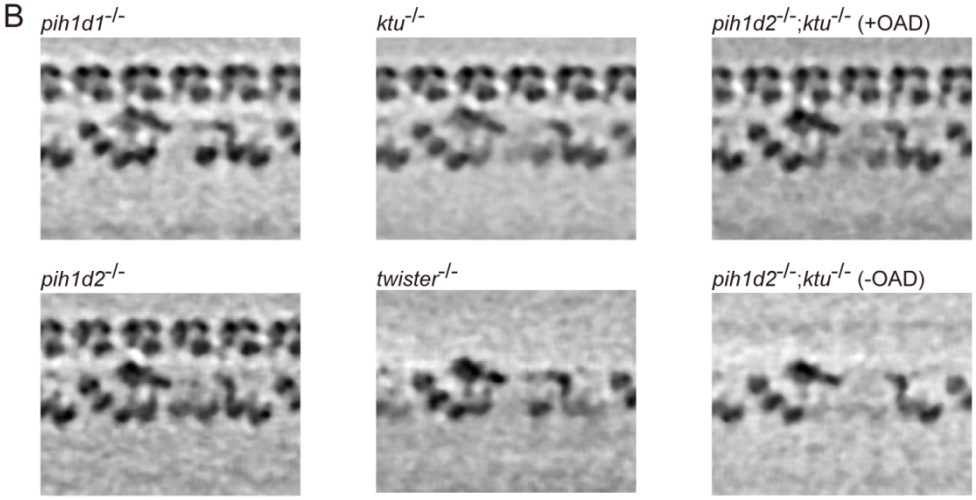

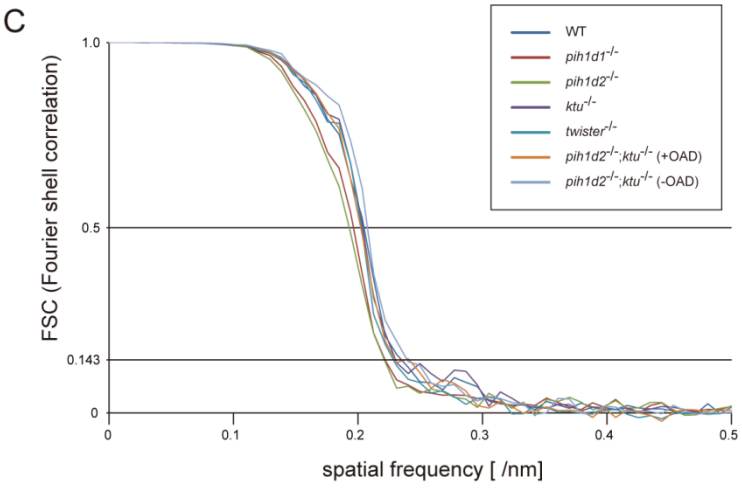

D

	Number of Particles	Resolution [Å]
WT	441	42.5
pih1d1$^{-/-}$	512	45.0
pih1d2$^{-/-}$	378	45.1
ktu$^{-/-}$	557	43.4
twister$^{-/-}$	510	43.7
pih1d2$^{-/-}$;*ktu*$^{-/-}$ (+OAD)	458	43.4
pih1d2$^{-/-}$;*ktu*$^{-/-}$ (-OAD)	551	41.7

Figure 13. Tomographic slices and Fourier shell correlations of the averaged subtomograms

(A) 2 nm-thick slices of the WT sperm subtomogram. Cross-section is shown on the left. Yellow line indicates the position of the right-hand slice and the slices in B. (B) 2

nm-thick slices of PIH gene mutant subtomograms. (C) Fourier shell correlation curves of the averaged subtomograms in this study. Effective resolutions were determined by a cutoff value of 0.143. (D) Number of particles and effective resolutions of the averaged subtomograms.

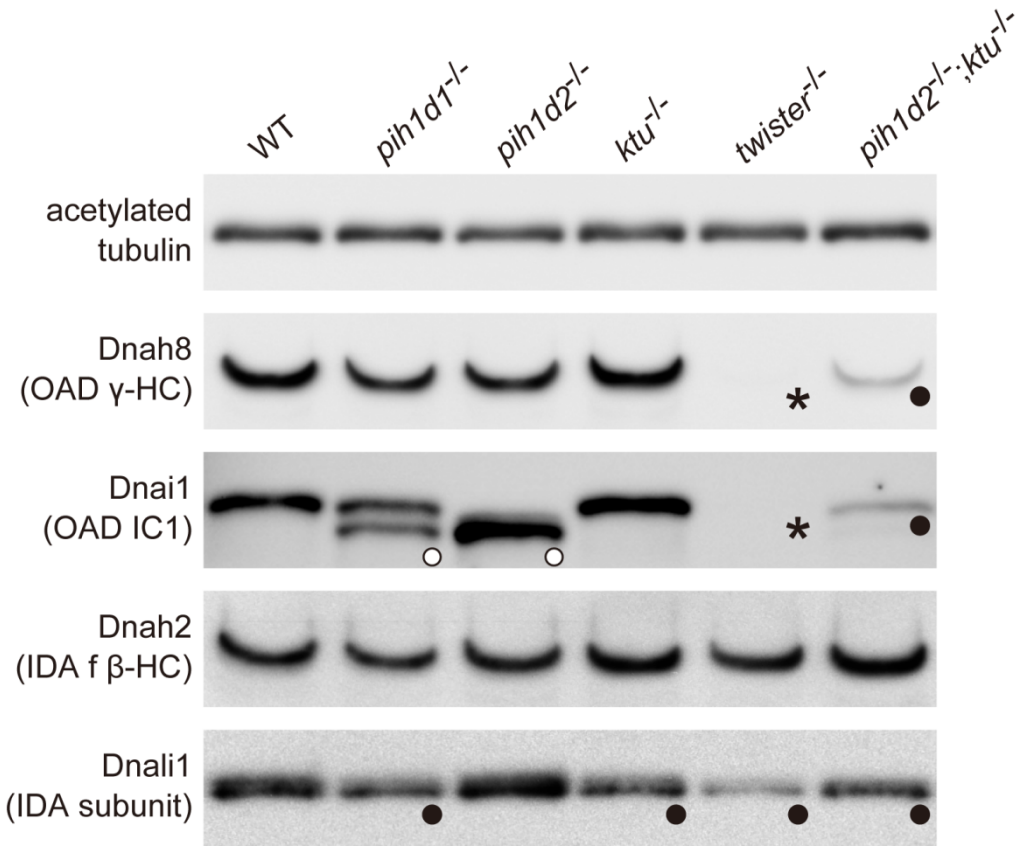

Figure 14. Immunoblot of axonemal dynein components

Immunoblot of sperm axonemes in WT and PIH gene mutants. Asterisks, filled circles, and open circles indicate missing, decreased, and shifted bands, respectively. Acetylated tubulin: control.

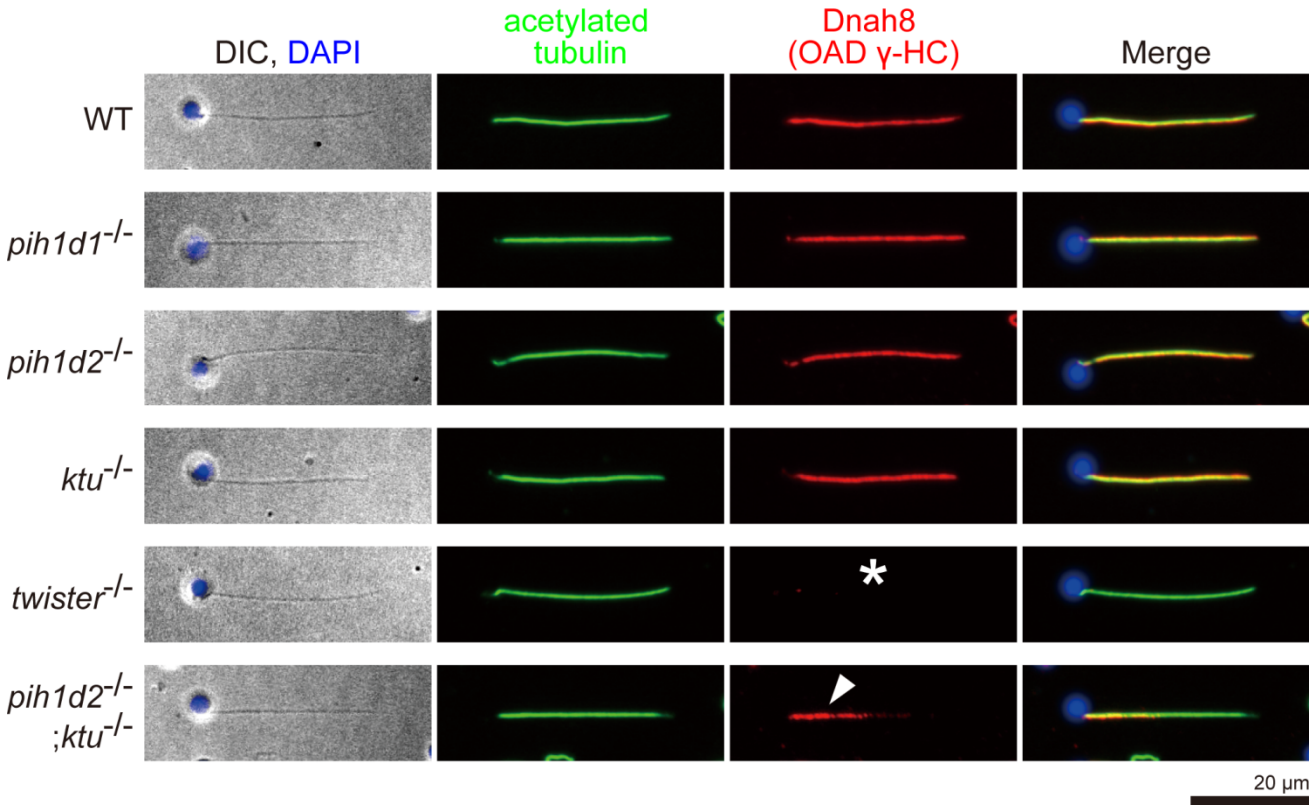

Figure 15. Immunofluorescence microscopy of sperm flagella

Immunofluorescence microscopy of zebrafish spermatozoa. Dnah8 was localized along the entire length of sperm flagella in WT, *pih1d1*$^{-/-}$, *pih1d2*$^{-/-}$, *ktu*$^{-/-}$. In *twister*$^{-/-}$, Dnah8 was lost (white asterisk), while in *pih1d2*$^{-/-}$;*ktu*$^{-/-}$, Dnah8 was localized only in the proximal half of the flagella (white arrowhead).

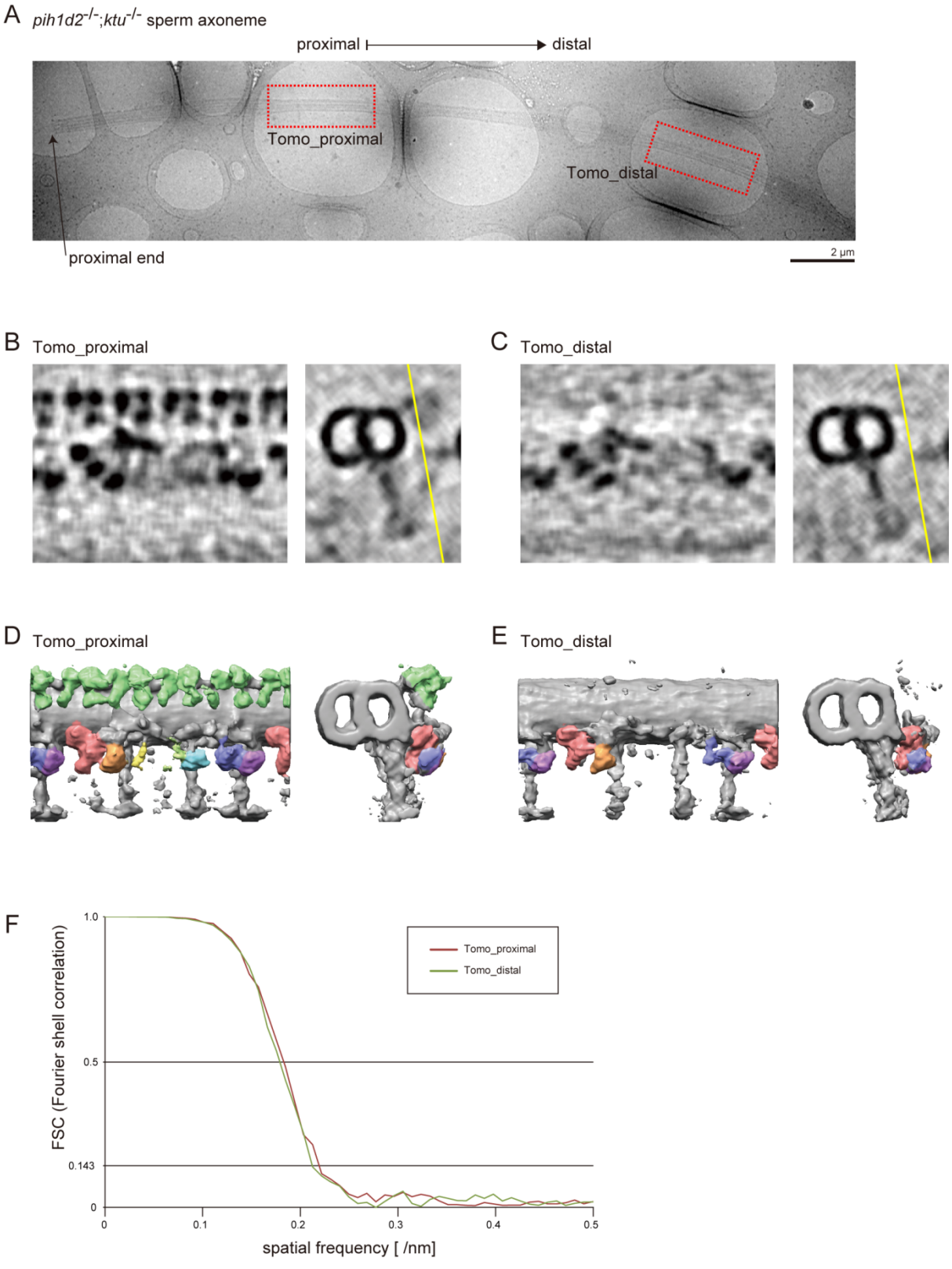

Figure 16. Axonemal structures in *pih1d2*$^{-/-}$;*ktu*$^{-/-}$ sperm

(A) Cryo-TEM image of *pih1d2*$^{-/-}$;*ktu*$^{-/-}$ axoneme, which was suitable for observing both proximal and distal regions by cryo-ET. Red squares indicate the observed areas. (B and C) 5 nm-thick slices of the subtomograms of the proximal (B; Tomo_proximal) and the distal (C; Tomo_distal) regions. Images on the left show slices of subtomograms at the point indicated by the yellow lines in the images on the right (cross-section). (D and E) 3D images of averaged subtomograms. Left: side views. Right: cross views. (F) Fourier shell correlation curves of the averaged subtomograms in this study. Number of particles: Tomo_proximal, 128; and Tomo_distal, 115. Effective resolutions were determined by a cutoff value of 0.143, and approximately 46 Å was estimated.

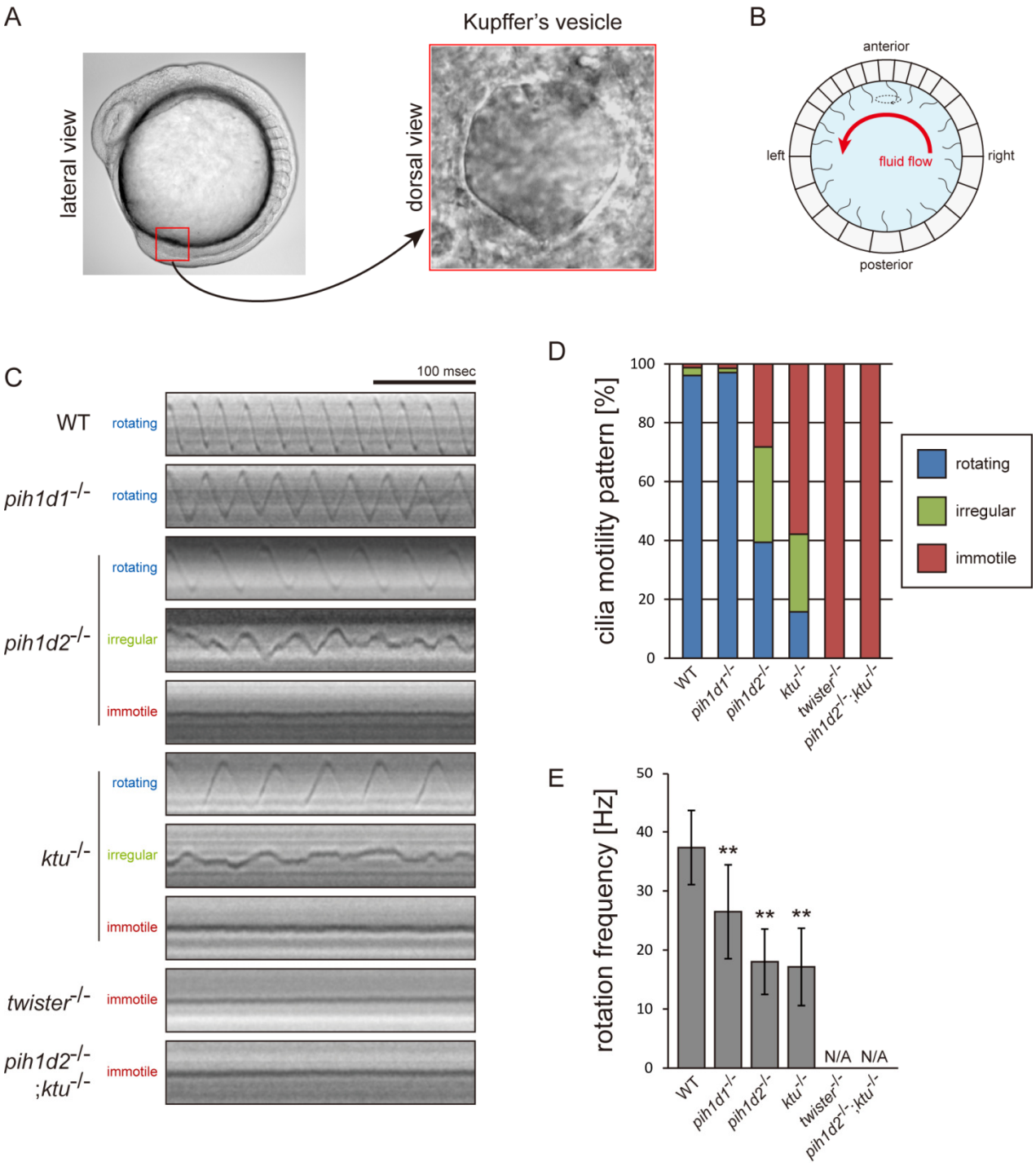

Figure 17. Mutations of PIH genes caused abnormal motilities of Kupffer's vesicle cilia

(A) Images of zebrafish embryo and Kupffer's vesicle. Red square in left-hand image indicates the position of the Kupffer's vesicle in a 12 hpf embryo. Right-hand image

shows the dorsal view of the Kupffer's vesicle. (B) Diagram of zebrafish Kupffer's vesicle. Mono-cilia, which project from epithelial cells, have rotational motilities to produce left-ward fluid flow (red arrow) in the organ. (C) Typical kymographs of Kupffer's vesicle cilia in WT and PIH gene mutants. Patterns of the kymographs were categorized into three classes: rotating (blue), irregular (green), and immotile (red). (D) Ratios of each motility class. Number of observed cilia: WT, 76; *pih1d1*$^{-/-}$, 67; *pih1d2*$^{-/-}$, 198; *ktu*$^{-/-}$, 190; *twister*$^{-/-}$, 53; and *pih1d2*$^{-/-}$;*ktu*$^{-/-}$, 48. (E) Rotational frequencies of Kupffer's vesicle cilia. Bar graphs show mean ± SD. **: p-value < 0.01 in Dunnett's test of each mutant against WT.

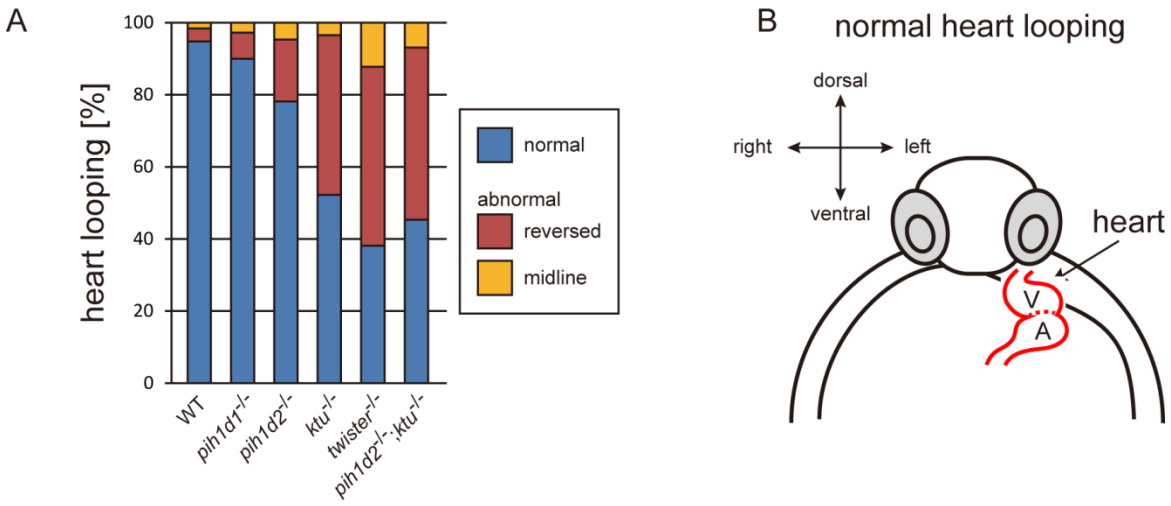

Figure 18. Mutations of PIH genes caused abnormal heart looping

(A) Heart looping of WT and mutant embryos at 30 hpf. Number of samples: WT, 247; *pih1d1*$^{-/-}$, 288; *pih1d2*$^{-/-}$, 275; *ktu*$^{-/-}$, 285; *twister*$^{-/-}$, 139; and *pih1d2*$^{-/-}$;*ktu*$^{-/-}$, 276. (B) Diagram represents normal heart looping of the 30 hpf embryo. V, ventricle; A, atrium.

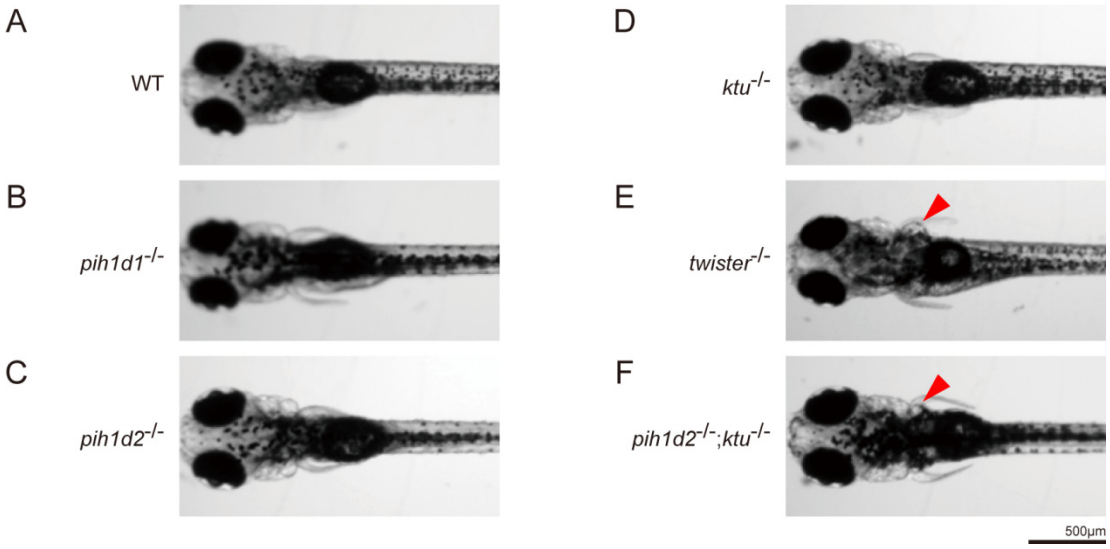

Figure 19. Expansion of pronephric duct was observed in *twister*$^{-/-}$ and *pih1d2*$^{-/-}$;*ktu*$^{-/-}$

(A-F) Dorsal views of zebrafish larvae at 4 days post-fertilization. (A) WT, (B) *pih1d1*$^{-/-}$, (C) *pih1d2*$^{-/-}$, (D) *ktu*$^{-/-}$, (E) *twister*$^{-/-}$, (F) *pih1d2*$^{-/-}$;*ktu*$^{-/-}$. *twister*$^{-/-}$ and *pih1d2*$^{-/-}$;*ktu*$^{-/-}$ exhibited abnormal expansions of pronephric ducts (red arrowheads), which disabled larvae from having their pectoral fins close to their bodies.

A

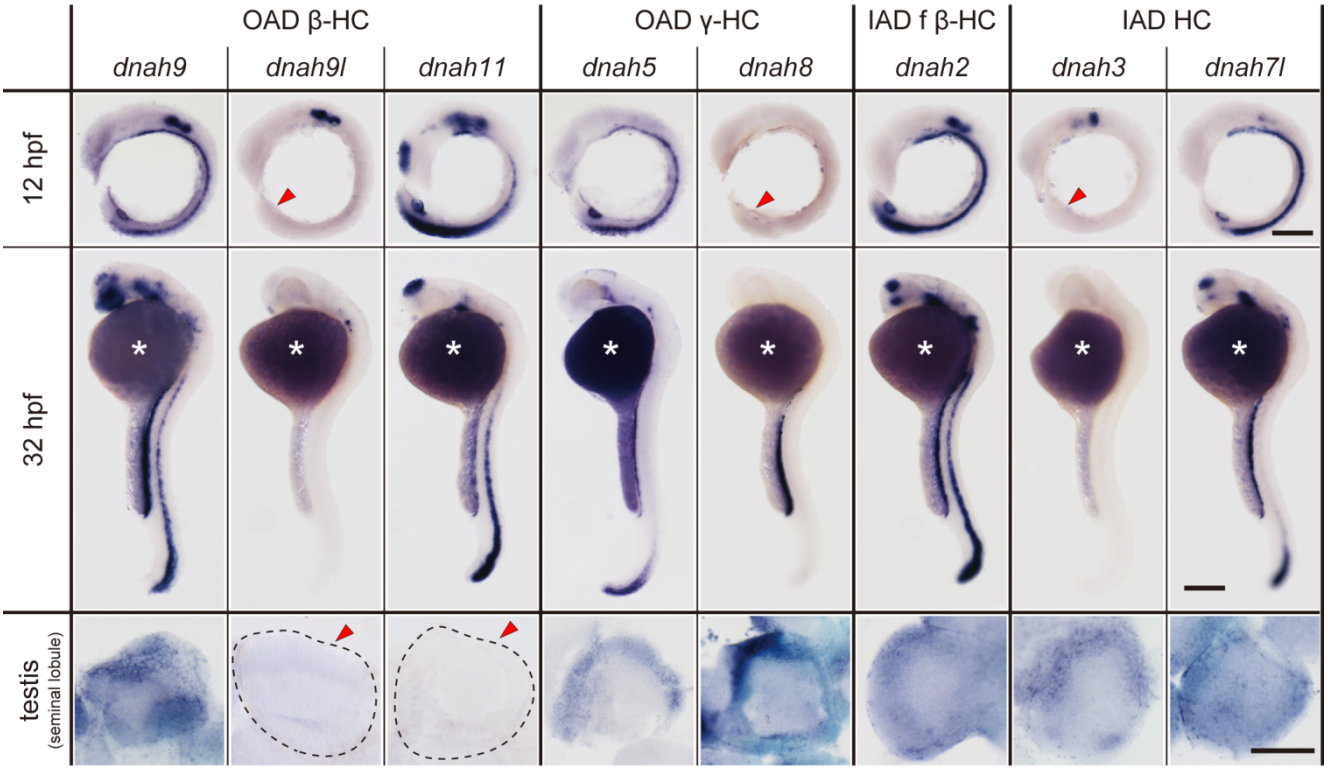

B

		gene expression	
		Kupffer's vesicle	testis
OAD β-HC	*dnah9*	+	+
	dnah9l	-	-
	dnah11	+	-
OAD γ-HC	*dnah5*	+	+
	dnah8	-	+
IAD f β-HC	*dnah2*	+	+
IAD HC	*dnah3*	-	+
	dnah7l	+	+

Figure 20. DNAH genes showed distinct expression patterns in zebrafish embryos and testis

(A) Whole-mount *in situ* hybridization of DNAH genes with embryos (12 and 32 hpf) and dissected testis (seminal lobule). For embryos, lateral views are shown. Yolk of 12

hpf embryos was removed before observation to show Kupffer's vesicle clearly. Red arrowheads indicate Kupffer's vesicles or testes in which DNAH gene expressions were not detected. White asterisks: non-specific staining of yolk. Scale bars: 200 μm for embryos; 100 μm for testes. (B) Comparison of DNAH gene expression between Kupffer's vesicle and testis. +, expressed; -, expression not detected. Red indicates when DNAH gene expression was difference between the two organs.

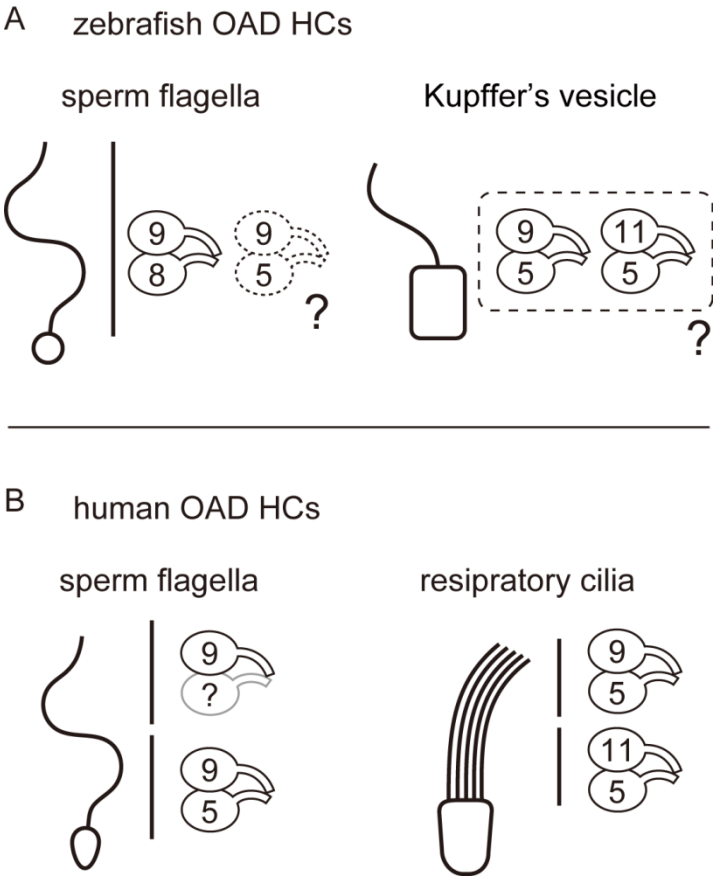

Figure 21. Organ-specific combinations of OAD HCs in zebrafish and human cilia/flagella

(A) Possible combinations of OAD HCs in zebrafish sperm flagella and Kupffer's vesicle cilia, suggested by the expression analysis of DNAH genes. Although testis showed expression of both γ-HC genes (*dnah5* and *dnah8*), Dnah8 were present along the entire length of sperm flagella, while the distribution of Dnah5 is not known. (B) Possible combinations of OAD HCs in human sperm flagella and respiratory cilia. Localizations of DNAH9 and DNAH5 in human spermatozoa were reported by Fliegauf et al. (2005). Localizations of DNAH9, DNAH11 and DNAH5 in human respiratory cilia were reported by Dougherty et al. (2016).

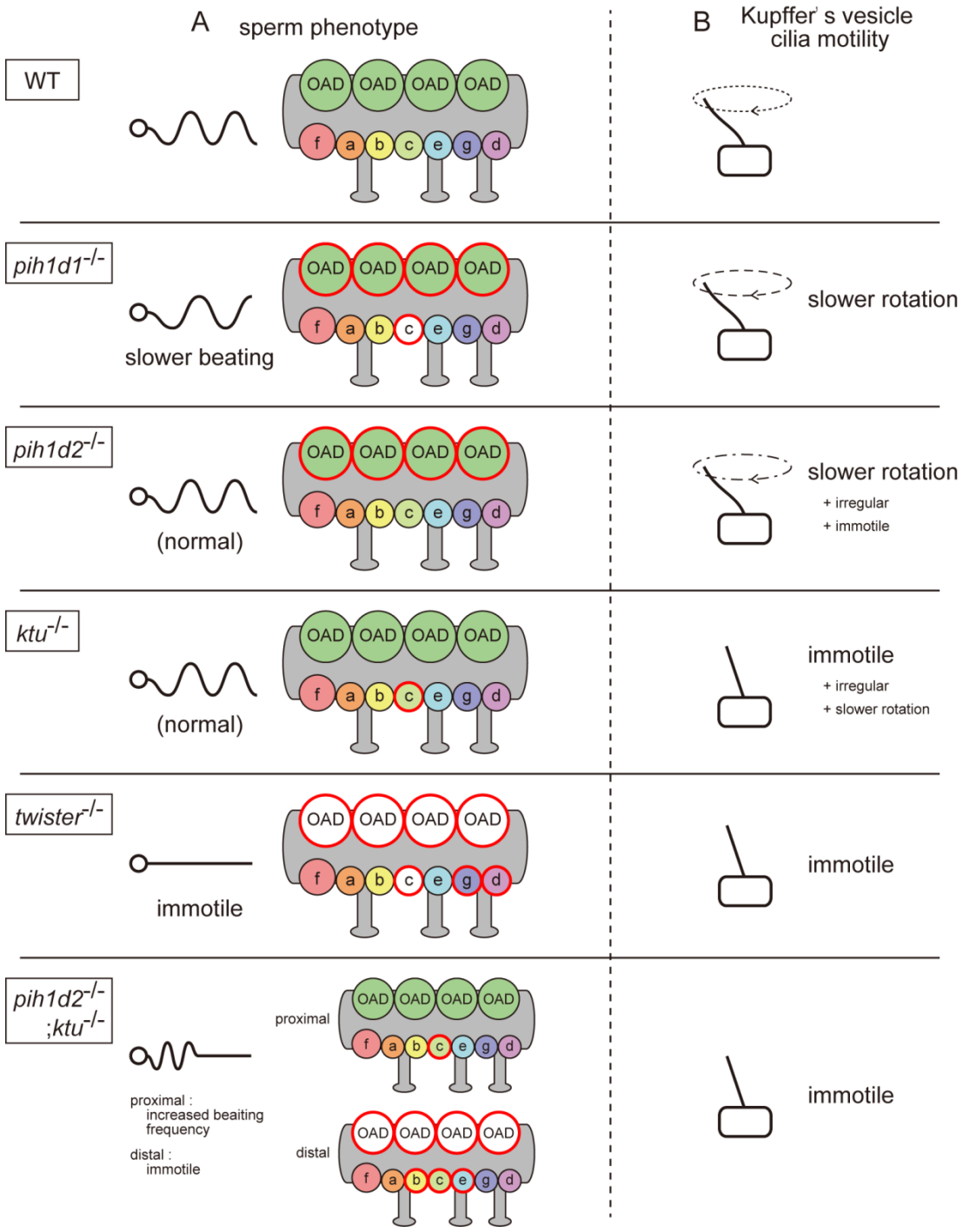

Figure 22. Summary of the ciliary phenotypes of PIH gene mutants

(A) Summary of the sperm motilities and the axonemal structures of WT and each PIH gene mutant. Abnormal axonemal dyneins are indicated by red circles filled with white (missing) or color (diminished or Dnai1 defects). (B) Summary of the motilities of Kupffer's vesicle cilia.

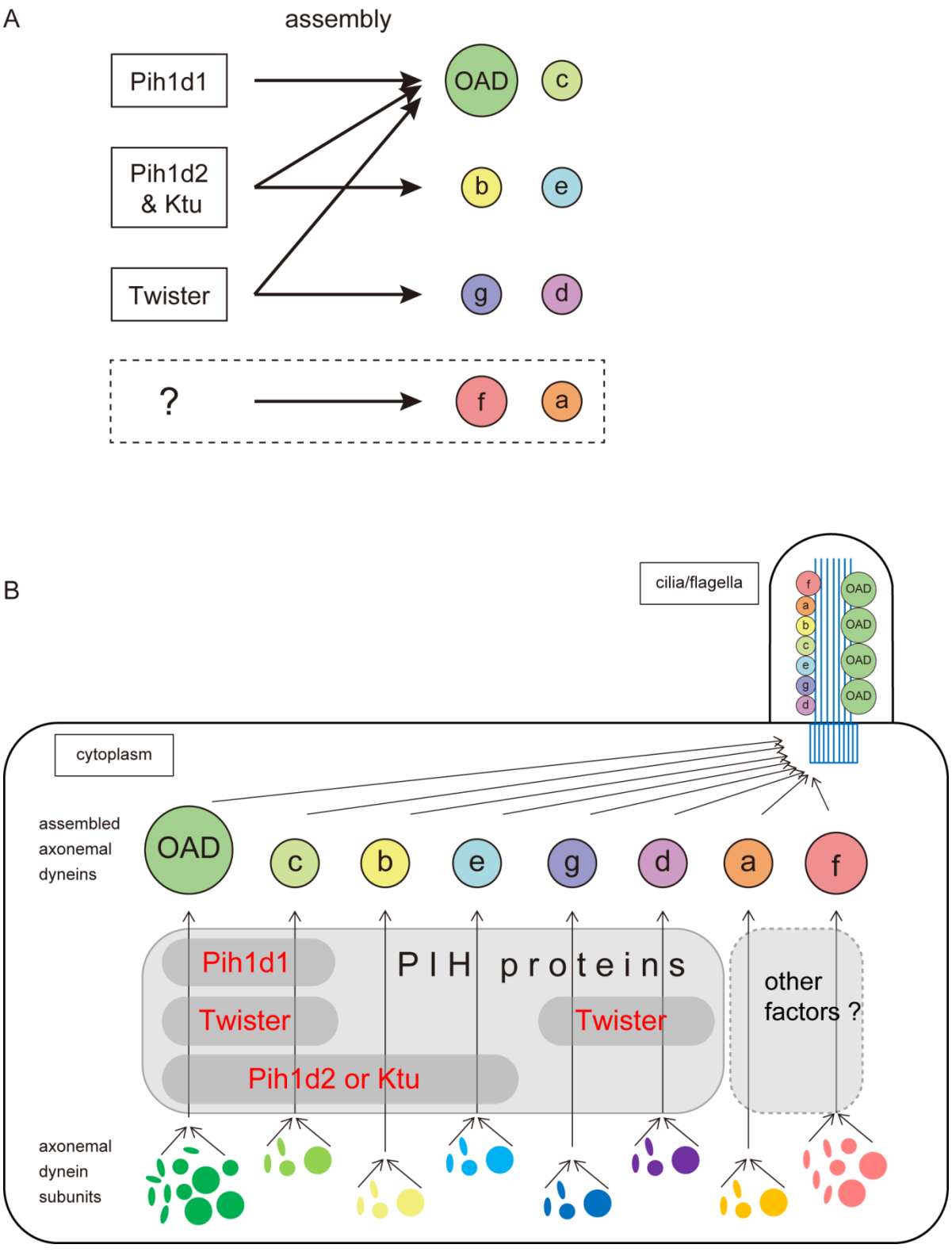

Figure 23. Proposed model of the axonemal dynein assembly by distinct PIH proteins

(A) Mutant phenotypes revealed axonemal dyneins assembled by distinct PIH proteins in zebrafish. Pih1d1 is required for the assembly of OAD and IAD c. Pih1d2 and Ktu are required for the assembly of OAD, IAD c, b and e. Twister are required for the assembly of OAD, IAD c, g and d. (B) Proposed model of the axonemal dynein assembly by distinct PIH proteins in the cytoplasm. Subunits of OAD, IAD c, b, e, g, and d are assembled through distinct PIH proteins, although factors responsible for the construction of IAD a or IAD f are not revealed in my research. Note that all PIH proteins are involved in the assembly of OAD and IAD c, suggesting stepwise assembly of these axonemal dyneins mediated by different PIH proteins.

References

Bedell, V.M., Y. Wang, J.M. Campbell, T.L. Poshusta, C.G. Starker, R.G. Krug, W. Tan, S.G. Penheiter, A.C. Ma, A.Y.H. Leung, S.C. Fahrenkrug, D.F. Carlson, D.F. Voytas, K.J. Clark, J.J. Essner, and S.C. Ekker. 2012. In vivo genome editing using a high-efficiency TALEN system. *Nature*. 491:114–8. doi:10.1038/nature11537.

Brown, J.M., and G.B. Witman. 2014. Cilia and Diseases. *Bioscience*. 64:1126–1137. doi:10.1093/biosci/biu174.

Bui, K.H., T. Yagi, R. Yamamoto, R. Kamiya, and T. Ishikawa. 2012. Polarity and asymmetry in the arrangement of dynein and related structures in the Chlamydomonas axoneme. *J. Cell Biol.* 198:913–25. doi:10.1083/jcb.201201120.

Dong, F., K. Shinohara, Y. Botilde, R. Nabeshima, Y. Asai, A. Fukumoto, T. Hasegawa, M. Matsuo, H. Takeda, H. Shiratori, T. Nakamura, and H. Hamada. 2014. Pih1d3 is required for cytoplasmic preassembly of axonemal dynein in mouse sperm. *J. Cell Biol.* 204:203–13. doi:10.1083/jcb.201304076.

Dougherty, G.W., N.T. Loges, J.A. Klinkenbusch, H. Olbrich, P. Pennekamp, T. Menchen, J. Raidt, J. Wallmeier, C. Werner, C. Westermann, C. Ruckert, V. Mirra, R. Hjeij, Y. Memari, R. Durbin, A. Kolb-Kokocinski, K. Praveen, M.A. Kashef, S. Kashef, F. Eghtedari, K. Häffner, P. Valmari, G. Baktai, M. Aviram, L. Bentur, I. Amirav, E.E. Davis, N. Katsanis, M. Brueckner, A. Shaposhnykov, G. Pigino, B. Dworniczak, and H. Omran. 2016. DNAH11 Localization in the Proximal Region of Respiratory Cilia Defines Distinct Outer Dynein Arm Complexes. *Am. J. Respir. Cell Mol. Biol.* 55:213–24. doi:10.1165/rcmb.2015-0353OC.

Essner, J.J., J.D. Amack, M.K. Nyholm, E.B. Harris, and H.J. Yost. 2005. Kupffer's

vesicle is a ciliated organ of asymmetry in the zebrafish embryo that initiates left-right development of the brain, heart and gut. *Development*. 132:1247–60. doi:10.1242/dev.01663.

Fliegauf, M., H. Olbrich, J. Horvath, J.H. Wildhaber, M.A. Zariwala, M. Kennedy, M.R. Knowles, and H. Omran. 2005. Mislocalization of DNAH5 and DNAH9 in respiratory cells from patients with primary ciliary dyskinesia. *Am. J. Respir. Crit. Care Med.* 171:1343–9. doi:10.1164/rccm.200411-1583OC.

Fok, A.K., H. Wang, A. Katayama, M.S. Aihara, and R.D. Allen. 1994. 22S axonemal dynein is preassembled and functional prior to being transported to and attached on the axonemes. *Cell Motil. Cytoskeleton*. 29:215–24. doi:10.1002/cm.970290304.

Fowkes, M.E., and D.R. Mitchell. 1998. The role of preassembled cytoplasmic complexes in assembly of flagellar dynein subunits. *Mol. Biol. Cell*. 9:2337–47.

Gagnon, J.A., E. Valen, S.B. Thyme, P. Huang, L. Akhmetova, L. Ahkmetova, A. Pauli, T.G. Montague, S. Zimmerman, C. Richter, and A.F. Schier. 2014. Efficient mutagenesis by Cas9 protein-mediated oligonucleotide insertion and large-scale assessment of single-guide RNAs. *PLoS One*. 9:e98186. doi:10.1371/journal.pone.0098186.

Gonzales, F.A., N.I.T. Zanchin, J.S. Luz, and C.C. Oliveira. 2005. Characterization of Saccharomyces cerevisiae Nop17p, a novel Nop58p-interacting protein that is involved in Pre-rRNA processing. *J. Mol. Biol.* 346:437–55. doi:10.1016/j.jmb.2004.11.071.

Hom, E.F.Y., G.B. Witman, E.H. Harris, S.K. Dutcher, R. Kamiya, D.R. Mitchell, G.J. Pazour, M.E. Porter, W.S. Sale, M. Wirschell, T. Yagi, and S.M. King. 2011. A unified taxonomy for ciliary dyneins. *Cytoskeleton (Hoboken)*. 68:555–65.

doi:10.1002/cm.20533.

Hoops, H.J., and G.B. Witman. 1983. Outer doublet heterogeneity reveals structural polarity related to beat direction in Chlamydomonas flagella. *J. Cell Biol.* 97:902–8.

Jiménez, A.J., M.-D. Domínguez-Pinos, M.M. Guerra, P. Fernández-Llebrez, and J.-M. Pérez-Fígares. 2014. Structure and function of the ependymal barrier and diseases associated with ependyma disruption. *Tissue barriers*. 2:e28426. doi:10.4161/tisb.28426.

Johnson, K.A., and J.L. Rosenbaum. 1992. Polarity of flagellar assembly in Chlamydomonas. *J. Cell Biol.* 119:1605–11.

Kagami, O., and R. Kamiya. 1992. Translocation and rotation of microtubules caused by multiple species of Chlamydomonas inner-arm dynein. *J. Cell Sci.* 103.

Kakihara, Y., and W.A. Houry. 2012. The R2TP complex: discovery and functions. *Biochim. Biophys. Acta*. 1823:101–7. doi:10.1016/j.bbamcr.2011.08.016.

Kamiya, R. 1995. Exploring the function of inner and outer dynein arms with Chlamydomonas mutants. *Cell Motil. Cytoskeleton*. 32:98–102. doi:10.1002/cm.970320205.

Kasahara, M., K. Naruse, S. Sasaki, Y. Nakatani, W. Qu, B. Ahsan, T. Yamada, Y. Nagayasu, K. Doi, Y. Kasai, T. Jindo, D. Kobayashi, A. Shimada, A. Toyoda, Y. Kuroki, A. Fujiyama, T. Sasaki, A. Shimizu, S. Asakawa, N. Shimizu, S.-I. Hashimoto, J. Yang, Y. Lee, K. Matsushima, S. Sugano, M. Sakaizumi, T. Narita, K. Ohishi, S. Haga, F. Ohta, H. Nomoto, K. Nogata, T. Morishita, T. Endo, T. Shin-I, H. Takeda, S. Morishita, and Y. Kohara. 2007. The medaka draft genome

and insights into vertebrate genome evolution. *Nature*. 447:714–9. doi:10.1038/nature05846.

Katoh, K., and D.M. Standley. 2013. MAFFT Multiple Sequence Alignment Software Version 7: Improvements in Performance and Usability. *Mol. Biol. Evol.* 30:772–780. doi:10.1093/molbev/mst010.

Kimmel, C.B., W.W. Ballard, S.R. Kimmel, B. Ullmann, and T.F. Schilling. 1995. Stages of embryonic development of the zebrafish. *Dev. Dyn.* 203:253–310. doi:10.1002/aja.1002030302.

Knowles, M.R., L.A. Daniels, S.D. Davis, M.A. Zariwala, and M.W. Leigh. 2013. Primary ciliary dyskinesia. Recent advances in diagnostics, genetics, and characterization of clinical disease. *Am. J. Respir. Crit. Care Med.* 188:913–22. doi:10.1164/rccm.201301-0059CI.

Kobayashi, D., and H. Takeda. 2012. Ciliary motility: the components and cytoplasmic preassembly mechanisms of the axonemal dyneins. *Differentiation.* 83:S23-9. doi:10.1016/j.diff.2011.11.009.

Kollmar, M. 2016. Fine-Tuning Motile Cilia and Flagella: Evolution of the Dynein Motor Proteins from Plants to Humans at High Resolution. *Mol. Biol. Evol.* 33:3249–3267. doi:10.1093/molbev/msw213.

Kramer-Zucker, A.G., F. Olale, C.J. Haycraft, B.K. Yoder, A.F. Schier, and I.A. Drummond. 2005. Cilia-driven fluid flow in the zebrafish pronephros, brain and Kupffer's vesicle is required for normal organogenesis. *Development*. 132:1907–21. doi:10.1242/dev.01772.

Kremer, J.R., D.N. Mastronarde, and J.R. McIntosh. 1996. Computer Visualization of

Three-Dimensional Image Data Using IMOD. *J. Struct. Biol.* 116:71–76. doi:10.1006/jsbi.1996.0013.

LeDizet, M., and G. Piperno. 1995. The light chain p28 associates with a subset of inner dynein arm heavy chains in Chlamydomonas axonemes. *Mol. Biol. Cell*. 6:697–711.

Li, Y., L. Zhao, S. Yuan, J. Zhang, and Z. Sun. 2017. Axonemal dynein assembly requires the R2TP complex component Pontin. *Development*. 144:4684–4693. doi:10.1242/dev.152314.

Lin, J., T. Heuser, B.I. Carbajal-González, K. Song, and D. Nicastro. 2012. The structural heterogeneity of radial spokes in cilia and flagella is conserved. *Cytoskeleton*. 69:88–100. doi:10.1002/cm.21000.

Lin, J., W. Yin, M.C. Smith, K. Song, M.W. Leigh, M.A. Zariwala, M.R. Knowles, L.E. Ostrowski, and D. Nicastro. 2014. Cryo-electron tomography reveals ciliary defects underlying human RSPH1 primary ciliary dyskinesia. *Nat. Commun.* 5:5727. doi:10.1038/ncomms6727.

Matsuo, M., A. Shimada, S. Koshida, Y. Saga, and H. Takeda. 2013. The establishment of rotational polarity in the airway and ependymal cilia: analysis with a novel cilium motility mutant mouse. *Am. J. Physiol. Lung Cell. Mol. Physiol.* 304:L736-45. doi:10.1152/ajplung.00425.2012.

Metlagel, Z., Y.S. Kikkawa, and M. Kikkawa. 2007. Ruby-Helix: an implementation of helical image processing based on object-oriented scripting language. *J. Struct. Biol.* 157:95–105. doi:10.1016/j.jsb.2006.07.015.

Mitchison, H.M., M. Schmidts, N.T. Loges, J. Freshour, A. Dritsoula, R.A. Hirst, C.

O'Callaghan, H. Blau, M. Al Dabbagh, H. Olbrich, P.L. Beales, T. Yagi, H. Mussaffi, E.M.K. Chung, H. Omran, and D.R. Mitchell. 2012. Mutations in axonemal dynein assembly factor DNAAF3 cause primary ciliary dyskinesia. *Nat. Genet.* 44:381–389. doi:10.1038/ng.1106.

Nicastro, D., C. Schwartz, J. Pierson, R. Gaudette, M.E. Porter, and J.R. McIntosh. 2006. The Molecular Architecture of Axonemes Revealed by Cryoelectron Tomography. *Science (80-.).* 313:944–948. doi:10.1126/science.1128618.

Nonaka, S., Y. Tanaka, Y. Okada, S. Takeda, A. Harada, Y. Kanai, M. Kido, and N. Hirokawa. 1998a. Randomization of left-right asymmetry due to loss of nodal cilia generating leftward flow of extraembryonic fluid in mice lacking KIF3B motor protein. *Cell*. 95:829–37.

Oda, T., H. Yanagisawa, and M. Kikkawa. 2015. Detailed structural and biochemical characterization of the nexin-dynein regulatory complex. *Mol. Biol. Cell*. 26:294–304. doi:10.1091/mbc.E14-09-1367.

Olcese, C., M.P. Patel, A. Shoemark, S. Kiviluoto, M. Legendre, H.J. Williams, C.K. Vaughan, J. Hayward, A. Goldenberg, R.D. Emes, M.M. Munye, L. Dyer, T. Cahill, J. Bevillard, C. Gehrig, M. Guipponi, S. Chantot, P. Duquesnoy, L. Thomas, L. Jeanson, B. Copin, A. Tamalet, C. Thauvin-Robinet, J.-F. Papon, A. Garin, I. Pin, G. Vera, P. Aurora, M.R. Fassad, L. Jenkins, C. Boustred, T. Cullup, M. Dixon, A. Onoufriadis, A. Bush, E.M.K. Chung, S.E. Antonarakis, M.R. Loebinger, R. Wilson, M. Armengot, E. Escudier, C. Hogg, S. UK10K Rare Group, S. Amselem, Z. Sun, L. Bartoloni, J.-L. Blouin, H.M. Mitchison, S. Bhattacharya, K. Carss, K. Chatterjee, S. Cirak, C. Cosgrove, D. Allan, R. Durbin, D. Fitzpatrick, J. Floyd, A.R. Foley, C. Franklin, M. Futema, S.E. Humphries, M. Hurles, S. McCarthy, D. Muddyman, F. Muntoni, V. Parker, F. Payne, V. Plagnol, L. Raymond, D.B. Savage, P.J. Scambler, M. Schmidts, R. Semple, E. Serra, J.

Stalker, M. van Kogelenberg, P. Vijayarangakannan, K. Walter, S. Amselem, Z. Sun, L. Bartoloni, J.-L. Blouin, and H.M. Mitchison. 2017. X-linked primary ciliary dyskinesia due to mutations in the cytoplasmic axonemal dynein assembly factor PIH1D3. *Nat. Commun.* 8:14279. doi:10.1038/ncomms14279.

Omran, H., D. Kobayashi, H. Olbrich, T. Tsukahara, N.T. Loges, H. Hagiwara, Q. Zhang, G. Leblond, E. O'Toole, C. Hara, H. Mizuno, H. Kawano, M. Fliegauf, T. Yagi, S. Koshida, A. Miyawaki, H. Zentgraf, H. Seithe, R. Reinhardt, Y. Watanabe, R. Kamiya, D.R. Mitchell, and H. Takeda. 2008. Ktu/PF13 is required for cytoplasmic pre-assembly of axonemal dyneins. *Nature*. 456:611–6. doi:10.1038/nature07471.

Paff, T., N.T. Loges, I. Aprea, K. Wu, Z. Bakey, E.G. Haarman, J.M.A. Daniels, E.A. Sistermans, N. Bogunovic, G.W. Dougherty, I.M. Höben, J. Große-Onnebrink, A. Matter, H. Olbrich, C. Werner, G. Pals, M. Schmidts, H. Omran, and D. Micha. 2017. Mutations in PIH1D3 Cause X-Linked Primary Ciliary Dyskinesia with Outer and Inner Dynein Arm Defects. *Am. J. Hum. Genet.* 100:160–168. doi:10.1016/j.ajhg.2016.11.019.

Pettersen, E.F., T.D. Goddard, C.C. Huang, G.S. Couch, D.M. Greenblatt, E.C. Meng, and T.E. Ferrin. 2004. UCSF Chimera--a visualization system for exploratory research and analysis. *J. Comput. Chem.* 25:1605–12. doi:10.1002/jcc.20084.

Piperno, G., Z. Ramanis, E.F. Smith, and W.S. Sale. 1990. Three distinct inner dynein arms in Chlamydomonas flagella: molecular composition and location in the axoneme. *J. Cell Biol.* 110:379–89.

Saitou, N., and M. Nei. 1987. The neighbor-joining method: a new method for reconstructing phylogenetic trees. *Mol. Biol. Evol.* 4:406–25.

Sakato, M., and S.M. King. 2004. Design and regulation of the AAA+ microtubule motor dynein. *J. Struct. Biol.* 146:58–71. doi:10.1016/j.jsb.2003.09.026.

San Agustin, J.T., G.J. Pazour, and G.B. Witman. 2015. Intraflagellar transport is essential for mammalian spermiogenesis but is absent in mature sperm. *Mol. Biol. Cell*. 26:4358–72. doi:10.1091/mbc.E15-08-0578.

Sun, Z., A. Amsterdam, G.J. Pazour, D.G. Cole, M.S. Miller, and N. Hopkins. 2004. A genetic screen in zebrafish identifies cilia genes as a principal cause of cystic kidney. *Development*. 131:4085–93. doi:10.1242/dev.01240.

Takao, D., and K.J. Verhey. 2016. Gated entry into the ciliary compartment. *Cell. Mol. Life Sci.* 73:119–127. doi:10.1007/s00018-015-2058-0.

Tarkar, A., N.T. Loges, C.E. Slagle, R. Francis, G.W. Dougherty, J. V Tamayo, B. Shook, M. Cantino, D. Schwartz, C. Jahnke, H. Olbrich, C. Werner, J. Raidt, P. Pennekamp, M. Abouhamed, R. Hjeij, G. Köhler, M. Griese, Y. Li, K. Lemke, N. Klena, X. Liu, G. Gabriel, K. Tobita, M. Jaspers, L.C. Morgan, A.J. Shapiro, S.J.F. Letteboer, D.A. Mans, J.L. Carson, M.W. Leigh, W.E. Wolf, S. Chen, J.S. Lucas, A. Onoufriadis, V. Plagnol, M. Schmidts, K. Boldt, R. Roepman, M.A. Zariwala, C.W. Lo, H.M. Mitchison, M.R. Knowles, R.D. Burdine, J.J. LoTurco, H. Omran, and H. Omran. 2013. DYX1C1 is required for axonemal dynein assembly and ciliary motility. *Nat. Genet.* 45:995–1003. doi:10.1038/ng.2707.

Ueno, H., T. Ishikawa, K.H. Bui, K. Gonda, T. Ishikawa, and T. Yamaguchi. 2012. Mouse respiratory cilia with the asymmetric axonemal structure on sparsely distributed ciliary cells can generate overall directional flow. *Nanomedicine*. 8:1081–7. doi:10.1016/j.nano.2012.01.004.

Viswanadha, R., E.L. Hunter, R. Yamamoto, M. Wirschell, L.M. Alford, S.K. Dutcher,

and W.S. Sale. 2014. The ciliary inner dynein arm, I1 dynein, is assembled in the cytoplasm and transported by IFT before axonemal docking. *Cytoskeleton (Hoboken)*. 71:573–86. doi:10.1002/cm.21192.

Wanner, A., M. Salathé, and T.G. O'Riordan. 1996. Mucociliary clearance in the airways. *Am. J. Respir. Crit. Care Med.* 154:1868–1902. doi:10.1164/ajrccm.154.6.8970383.

Wilson-Leedy, J.G., and R.L. Ingermann. 2007. Development of a novel CASA system based on open source software for characterization of zebrafish sperm motility parameters. *Theriogenology*. 67:661–72. doi:10.1016/j.theriogenology.2006.10.003.

Wloga, D., D.M. Webster, K. Rogowski, M.-H. Bré, N. Levilliers, M. Jerka-Dziadosz, C. Janke, S.T. Dougan, and J. Gaertig. 2009. TTLL3 Is a Tubulin Glycine Ligase that Regulates the Assembly of Cilia. *Dev. Cell*. 16:867–876. doi:10.1016/j.devcel.2009.04.008.

Woolley, D.M. 1997. Studies on the eel sperm flagellum. I. The structure of the inner dynein arm complex. *J. Cell Sci.* 110 (Pt 1):85–94.

Woolley, D.M. 1998. Studies on the eel sperm flagellum. 3. Vibratile motility and rotatory bending. *Cell Motil. Cytoskeleton*. 39:246–55. doi:10.1002/(SICI)1097-0169(1998)39:3<246::AID-CM7>3.0.CO;2-2.

Yagi, T., K. Uematsu, Z. Liu, and R. Kamiya. 2009. Identification of dyneins that localize exclusively to the proximal portion of Chlamydomonas flagella. *J. Cell Sci.* 122:1306–1314. doi:10.1242/jcs.045096.

Yamamoto, R., M. Hirono, and R. Kamiya. 2010. Discrete PIH proteins function in the

cytoplasmic preassembly of different subsets of axonemal dyneins. *J. Cell Biol.* 190:65–71. doi:10.1083/jcb.201002081.

Yamamoto, R., J.M. Obbineni, L.M. Alford, T. Ide, M. Owa, J. Hwang, T. Kon, K. Inaba, N. James, S.M. King, T. Ishikawa, W.S. Sale, and S.K. Dutcher. 2017. Chlamydomonas DYX1C1/PF23 is essential for axonemal assembly and proper morphology of inner dynein arms. *PLOS Genet.* 13:e1006996. doi:10.1371/journal.pgen.1006996.

Zhao, R., M. Davey, Y.-C. Hsu, P. Kaplanek, A. Tong, A.B. Parsons, N. Krogan, G. Cagney, D. Mai, J. Greenblatt, C. Boone, A. Emili, and W.A. Houry. 2005. Navigating the Chaperone Network: An Integrative Map of Physical and Genetic Interactions Mediated by the Hsp90 Chaperone. *Cell*. 120:715–727. doi:10.1016/j.cell.2004.12.024.

Acknowledgments

I would like to express my deepest and sincere gratitude to my supervisors, Dr. Hiroyuki Takeda and Dr. Masahide Kikkawa, for providing me with the opportunity to study in a splendid environment. Without their substantial supports and great patience, this thesis would not have been materialized.

I would like to express my great gratitude to Dr. Toshiyuki Oda and Dr. Haruaki Yanagisawa for their substantial support in developing the method to analyze zebrafish sperm structure using cryo-ET.

I would like to express my sincere appreciation to Dr. Tatsuya Tsukahara and Dr. Sumito Koshida for their valuable suggestions and experimental supports at the start of my study. I also thank Dr. Cheol-Hee Kim for his help in zebrafish TALEN genome-editing.

I am truly grateful to the members of Takeda Laboratory and Kikkawa Laboratory for all they have done for my life in these laboratories.

Finally, I am greatly indebted to my parents for their warm support and generous affection. I dedicate this doctoral thesis to them.